

# Triboelectric nanogenerators for energy harvesting in tires

Master's thesis in Complex Adaptive Systems

Vincent Udén

DEPARTMENT OF MECHANICS AND MARITIME SCIENCES

---

CHALMERS UNIVERSITY OF TECHNOLOGY  
Gothenburg, Sweden 2024  
[www.chalmers.se](http://www.chalmers.se)



MASTER'S THESIS IN COMPLEX ADAPTIVE SYSTEMS

**Triboelectric nanogenerators for  
energy harvesting in tires**

Vincent Udén



**CHALMERS**  
UNIVERSITY OF TECHNOLOGY

Department of Mechanics and Maritime Sciences  
Division of Division Name  
CHALMERS UNIVERSITY OF TECHNOLOGY  
Gothenburg, Sweden 2024

Triboelectric nanogenerators for energy harvesting in tires  
Vincent Udén

© Vincent Udén, 2024.

Supervisor: Henrik Staaf, RISE Sensorsystem Examiner: Peter Folkow, Department of Mechanics and Maritime Sciences

Master's Thesis 2024  
Department of Mechanics and Maritime Sciences  
Chalmers University of Technology  
SE-412 96 Gothenburg  
Sweden  
Telephone +46 31 772 1000

Cover: A grated sliding mode triboelectric nanogenerator which was tested in a tire.

Typeset in L<sup>A</sup>T<sub>E</sub>X  
Gothenburg, Sweden 2024

Triboelectric nanogenerators for energy harvesting in tires

Vincent Udén

Department of Mechanics and Maritime Sciences

Division of Dynamics

Chalmers University of Technology

## Abstract

The advancement of portable, miniaturized electronics necessitates the development of sustainable power sources to ensure their widespread and efficient use. Energy harvesting, which involves converting ambient energy from the environment into usable electrical power, presents a promising solution to this challenge. This thesis focuses on exploring triboelectric nanogenerators (TENG) as a means of harvesting energy from the deformation of car tires under load.

This thesis details an investigation conducted through a combination of numerical models and physical experiments to assess the performance of TENGs. Initial tests involved evaluating TENGs in isolation to understand their fundamental energy harvesting capabilities. Subsequently, TENGs were mounted in car tires and tested under realistic working loads to simulate actual driving conditions.

Aluminum electrodes were found to produce more current than copper electrodes for most dielectric materials tested. Films of  $25\text{ }\mu\text{m}$  thick Kapton and FEP, particularly when used with aluminum electrodes, demonstrated the highest power outputs of the tested dielectrics. A thicker  $127\text{ }\mu\text{m}$  FEP film also performed well as a dielectric layer.

Despite the advancements made, none of the prototype TENGs constructed during this project achieved the necessary power output in the desired mW range. However, the prototypes demonstrated currents of up to  $375\text{ nA}$  and voltages reaching  $75\text{ V}$ , resulting in an approximate power output of  $25\text{ }\mu\text{W}$ . These findings suggest that, with further optimization, sliding mode TENGs have the potential to achieve the desired power output, paving the way for their practical application in sustainable energy harvesting for electronic devices.

**Keywords:** Triboelectricity, Triboelectric nanogenerators, TENG, Energy harvesting, Tires



# Acknowledgements

Before diving into the depths of niche physical phenomena I want to acknowledge and thank the people in my life who have paved the way for me to rub plastic pieces together for half a year, hoping to find electricity along the way.

First off I want to thank Cristina Rusu for providing, leading and allowing me to be a part of the Energy ECS UC5 project. You have given me nothing but support and encouragement from day one, allowing me to believe in my ability through the entire project without the need for doubts or hesitation. I also want to extend my gratitude to my examiner Peter Folkow for agreeing to oversee the work I have done, making sure the completed project is the best version it could possible become.

Henrik, you have not only supported me throughout this *very* open-ended project but you are a massive part of why I am even here in the first place, soon to have an entire master's degree as some sort of receipt of my ability. I am very lucky to have been as annoying and provocative as I was, all the way back at IT-Gymnasiet to have caught your attention.

Prior to even making it to the end of this master's programme I had to survive 4.5 years of studies at *Teknisk fysik*, an impossible task if not for the friends I made along the way. A special thanks goes out to my amazing friends of *FnollK 2021*. Our year together was challenging but rewarding and for every year that passes I grow increasingly thankful to have you all as my friends.

My studies have not only been a challenge for myself, but also to the people around me. Every hour in the lab is an hour away from home, regardless of how much I enjoy experimenting. Thank you, to my amazing partner Ida. Thank you for putting up with all the hours I have spent on my education. Thank you for putting up with all the antics I get up to. Thank you for supporting me every single step of the way. I hope to never take that for granted.

Finally we have arrived at my beginning, my foundation, my heritage. Thank you to my family. My mother, father and brother. Thank you to all of my extended family. You all contributed an immeasurable part in shaping me to be the person I am. Having a home which not only let me study, train and have fun, but actively encouraged me to do so is the biggest privilege anyone could have.



# Nomenclature

Below is the nomenclature of parameters and variables that have been used throughout this thesis.

## Acronyms

FEP	Fluorinated ethylene propylene
PEEK	Polyether ether ketone
PP	Polypropylene
TENG	Triboelectric nanogenerator

## Mechanical Parameters

$b$	(Tire) Carcass width
$h$	Carcass thickness
$A_{CS}$	Carcass cross-section area
$\rho$	Tire density
$EI$	Carcass bending stiffness
$R$	Tire radius
$k_w$	Equivalent radial stiffness
$k_v$	Equivalent tangential stiffness
$p_0$	Inflation pressure
$\Omega$	Angular velocity
$F$	Normal force against tire surface

## Electrical Parameters

$R_{ext}$	External circuit resistance
-----------	-----------------------------

---

$\sigma$	Density of charges created using contact electrification (Triboelectric charge density)
$W$	TENG width (perpendicular to the coordinate $x$ )
$L$	TENG length (parallel to the coordinate $x$ )
$\delta$	Effective dielectric constant

## Variables

$n$	Order of modal expansion
$\lambda_n$	Modal participation factor
$m_n$	Modal equivalent mass
$g_n$	Modal damping factor
$k_n$	Modal stiffness factor
$\sigma_0$	Pre-load tension
$x(t)$	TENG actuation tangent to the tire surface
$z(t)$	TENG actuation perpendicular to the tire surface
$r$	A polar coordinate in the radial direction
$\varphi$	A polar coordinate perpendicular to the radial direction
$A$	Non-dimensionalising electrical constant
$H(t)$	Dimensionless induced charge

# Contents

<b>Nomenclature</b>	<b>viii</b>
<b>1 Introduction</b>	<b>1</b>
1.1 Background . . . . .	1
1.2 Purpose . . . . .	2
1.3 Goals . . . . .	2
1.4 Limitations . . . . .	2
<b>2 Theory</b>	<b>3</b>
2.1 The triboelectric effect . . . . .	3
2.1.1 Sliding mode . . . . .	4
2.1.2 Contact mode . . . . .	5
2.2 Mechanical analysis . . . . .	6
2.2.1 Tire Deformation . . . . .	7
2.2.2 Harvester Response . . . . .	9
2.3 Circuit analysis . . . . .	11
2.3.1 Nondimensionalising the contact mode . . . . .	13
2.3.2 Nondimensionalising the sliding mode . . . . .	15
<b>3 Methods</b>	<b>17</b>
3.1 Simulations . . . . .	17
3.1.1 Mechanical simulations . . . . .	17
3.1.2 Electrical simulations . . . . .	18
3.2 Physical experiments . . . . .	18
3.2.1 Experiments at RISE . . . . .	18
3.2.1.1 TENG voltage . . . . .	19
3.2.1.2 Robotic actuation . . . . .	19
3.2.1.3 TENG current . . . . .	20
3.2.1.4 TENG capacitance . . . . .	20
3.2.1.5 Reverse taping . . . . .	20
3.2.1.6 Grated sliding TENG . . . . .	20
3.2.1.7 Sliding direction . . . . .	21
3.2.1.8 Material selection . . . . .	21
3.2.2 Experiments at Nokian Tyres . . . . .	21

3.2.2.1	Modified contact mode TENG . . . . .	22
3.2.2.2	Grated sliding mode TENG . . . . .	23
<b>4 Results</b>		<b>25</b>
4.1 Simulations . . . . .		25
4.1.1 Mechanical simulations . . . . .		26
4.1.2 Electrical simulations . . . . .		28
4.2 Physical experiments . . . . .		30
4.2.1 Experiments at RISE . . . . .		30
4.2.1.1 TENG voltage . . . . .		30
4.2.1.2 Robotic actuation . . . . .		31
4.2.1.3 TENG current . . . . .		32
4.2.1.4 TENG capacitance . . . . .		33
4.2.1.5 Reverse taping . . . . .		34
4.2.1.6 Grated sliding TENG . . . . .		35
4.2.1.7 Sliding direction . . . . .		35
4.2.1.8 Material selection . . . . .		36
4.2.2 Experiments at Nokian Tyres . . . . .		37
4.2.2.1 Modified contact mode TENG . . . . .		37
4.2.2.2 Grated sliding mode TENG . . . . .		38
<b>5 Discussion</b>		<b>41</b>
5.1 Simulations . . . . .		41
5.1.1 Mechanical simulations . . . . .		41
5.1.2 Electrical simulations . . . . .		41
5.2 Physical experiments . . . . .		42
5.2.1 Experiments at RISE . . . . .		43
5.2.2 Experiments at Nokian Tyres . . . . .		43
<b>6 Conclusion</b>		<b>45</b>
<b>7 Future work</b>		<b>47</b>
<b>Bibliography</b>		<b>I</b>

# 1

## Introduction

### 1.1 Background

Advancements in integrated circuits over the past few decades have opened the door to an era of miniaturized electronics that are more portable and autonomous than ever before. These technologies require power solutions that are sustainable, maintenance-free, and renewable which limits the use of conventional power sources such as batteries. In this context, energy harvesting techniques that can capture and convert energy from the environment have emerged as a promising alternative [1, 2].

In general, energy harvesting refers to extracting high-quality (low entropy) energy from low-quality (high entropy) energy present in the environment. Such energy sources include thermal gradients, chaotic motion, electromagnetic radiation, vibrations and others [3]. Their high entropy implies irregular energy flows which is in stark contrast to conventional electric generation which rely on a steady energy input such as spinning turbines.

There is always some leakage of energy when powering a device or machine through conventional power sources. In other words the efficiency of a system is never 100% for any real applications of technology as some quantity always dissipates through heat or other high-entropy means. This creates an opportunity to scavenge some of the lost energy through means of harvesting to power low-energy electronics such as sensors.

Energy harvesting is especially useful when dissipatory mechanism **and** the sensor in need of power are situated far from the main power source. In this scenario a sensor could be powered by harvesting wasted energy as opposed to transporting electricity a large distance from the main power source.

One such scenario has been identified by RISE Research Institutes of Sweden in conjunction with Nokian Tires. Modern tires require a Tire Pressure Monitoring System (TPMS) mandated by law to provide feedback on pressure to the car they are mounted on. Current solutions feature low-energy electronics powered by a (non-rechargeable) battery large enough to last 5-10 years, the lifetime of the tire itself

[4]. The batteries measure capacities of several hundred mAh which significantly increase the weight and size of said sensor systems.

Powering the sensors centrally from the car is not an option as tires rotate freely around their mounting point and are subjected to large forces during operation, preventing the use of slip rings or other means of electrifying the tire [4]. These large forces are however a promising opportunity for energy harvesting which could replace the attached battery, providing more power with a lighter and perpetual power source.

## 1.2 Purpose

The main purpose of the work leading to this thesis is to understand and characterise the generation of electric energy from TENGs mounted to tires under realistic working conditions.

## 1.3 Goals

On the path to improving implementation of TENGs in tires for energy harvesting there are multiple sub-goals required to do so.

1. Model the dynamics of a rotating, deforming tire under realistic loads
2. Model the electrical response of a TENG to mechanical deformations
3. Combine the two models to estimate important performance numbers from design parameters

## 1.4 Limitations

Numerical simulations will be concerned with parameters present in real life conditions for tires associated with transportation by car. This implies per-tire loads in the 1000-5000 kN range, velocities from 10 to 120 km/h and integration of the TENG into a simple circuit with external loads ranging from 1 M $\Omega$  to 10 G $\Omega$ .

Furthermore it is assumed that the car is travelling in a straight line without accelerating or breaking which eliminates lateral and longitudinal loads on the tire carcass leaving. What remains are purely transversal loads which in the reference frame of a tire is equivalent to radial loads.

# 2

## Theory

There are several distinct but coupled theoretical aspects that need to be considered when creating a model for the behaviour of TENGs mounted to tires.

First of all a framework for understanding the triboelectric effect is required to understand where opportunities for energy harvesting might occur.

Subsequently the mechanics of the tire and the mounted energy harvester need to be analysed. *How does the tire move in response to its environment? How does the harvester in turn respond to the movement of the tire?*

To combine the two a firm understanding of the electrical response of the TENG to the induced mechanical displacement is needed and how this response acts in a simple circuit.

A TENG does act as a electromechanical transducer in some respects [5] giving rise to a mechanical reaction force due to electrical processes. However this coupling between electrical and mechanical responses is negligible and can be ignored as will be shown later in figure 4.6. For now it is satisfactory to conclude that the two aspects can be studied independent of each other.

### 2.1 The triboelectric effect

Triboelectricity is a common but poorly understood effect on a fundamental level. It is still an open question as to why it occurs [6, 7] even though the resulting effect is agreed upon.

The triboelectric effect is a charge transfer that occurs when two surfaces make contact. In colloquial terms it can be described by a “willingness” of one surface to donate charges (which might be electrons or ions) to another during physical contact. This “willingness” is in stricter terms thought to be some combination of an electronegativity and work function inherent to the material [8].

Electronegativity can be defined as “the power of an atom in a molecule to attract

## 2. Theory

---

electrons to itself” [9]. The work function on the other hand is defined as “the energy necessary to remove an electron at the Fermi level (of a material)” [10]. These are related but no concrete relationship has been established between the two due to the inherent vagueness of the first definition [9].

Exactly what is meant by *contact* and *surface* on a microscopic level is not well defined, especially not in relation to contact charging [11]. What is macroscopically thought of as a surface does not exist on the atomic level as irregularities and imperfections cloud the definition of what is considered belonging to or being outside of the material in question. Defining contact on a microscopic level also proves difficult due to surface irregularities giving rise to questions such as how much of two surfaces need to be in contact before they are considered to be in contact as a totality.

All of this is to say that an attempt to derive and describe triboelectricity from first principles is futile for the scope of this work, thus macroscopic, effective models are used.

Contact charging via the triboelectric effect comes in three distinct modes. The sliding mode occurs when two materials are rubbed against each other, most commonly known by rubbing a balloon against human hair to produce static electricity.

The contact mode is in action when two materials are repeatedly brought into and out of contact without sliding against each other. Usually this would occur in a motion perpendicular to both surfaces. This allows for harvesting of motions which might be difficult to transform into sliding along the surfaces.

Freestanding mode is similar in nature to the sliding mode but requires no contact between materials. Charges are instead transferred from the air surrounding a dielectric material through friction with the air. This mode produces significantly less energy than the two alternatives [12] and as such will not be considered here.

### 2.1.1 Sliding mode

A TENG functions as a transducer, converting the relative displacement of two parts into electric voltage. Charges are transferred from one dielectric to another by means of the triboelectric effect during tangential rubbing of the two. These generated surface charges in turn attract or repel electrons in the respective electrode on which they are mounted. A schematic of how this is used to generate electricity over an external load can be seen in figure 2.1.

Since triboelectricity only acts on the surfaces of objects, the induced triboelectric charges shown in figure 2.1 are only present on the exposed surfaces. In the overlapping region the charges cancel thus forming no macroscopic electrical field.

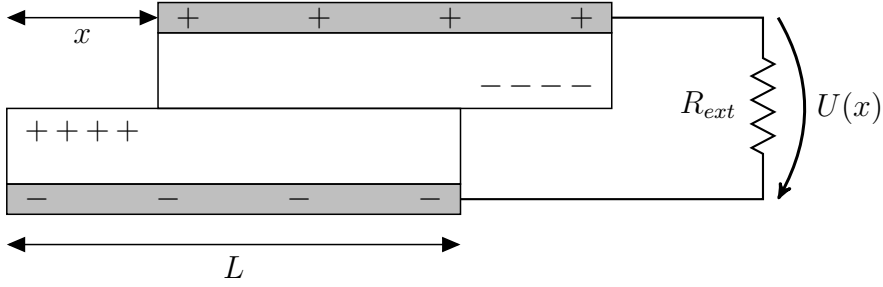


**Figure 2.1:** A typical sliding mode harvester. Two dielectric (white) materials sliding against each other attached to an electrode (gray) on each side. The electrodes are connected through an external load  $R_{ext}$ .

At open circuit conditions ( $R_{ext} = \infty$ ) the induced voltage is described by

$$U_{OC} = \frac{\sigma x}{\varepsilon_0(L-x)} \left( \frac{\varepsilon_0 d_1}{\varepsilon_1} + \frac{\varepsilon_0 d_2}{\varepsilon_2} \right) \quad (2.1)$$

where  $\sigma$  is the triboelectric charge density,  $x$  is the relative displacement of the two plates,  $L$  is the length of the plates,  $d_1, d_2$  are the thicknesses of the respective dielectrics and  $\varepsilon_1, \varepsilon_2$  are their respective electric permittivity [13].

Often it is practical to group the dielectric constants and permittivities into a single *effective dielectric constant*

$$\delta = \frac{\varepsilon_0 d_1}{\varepsilon_1} + \frac{\varepsilon_0 d_2}{\varepsilon_2}. \quad (2.2)$$

It is possible to construct a TENG with a single dielectric sliding (or contacting) directly against the other electrode. In that case  $d_2/\varepsilon_2 = 0$ .

When characterising the parameters of a harvester it can be useful to know the induced charges on the surfaces of the dielectrics (referred to as triboelectric charges) which are given by

$$Q_{SC} = \sigma W x \quad (2.3)$$

where  $W$  is the width of the plates (perpendicular to  $x$  and  $z$ ) [13].

As the harvester is constructed from two parallel plates in close vicinity it acts as a capacitor in addition to inducing current. Using a parallel-plate capacitor model and assuming no capacitive effect in the non-overlapping regions the capacitance can be expressed as [14]

$$C_{teng} = \frac{\varepsilon_0 W (L-x)}{\delta}. \quad (2.4)$$

### 2.1.2 Contact mode

Similar to the sliding mode, contact mode allows a TENG to convert relative plate displacement into electric voltage. The primary difference lies in the direction of this displacement. In this setup the harvester instead makes use of motion perpendicular

to the dielectric plates by letting them make repeated contact, each time transferring charges from one onto the other. A schematic of the contact mode configuration can be seen in figure 2.2.

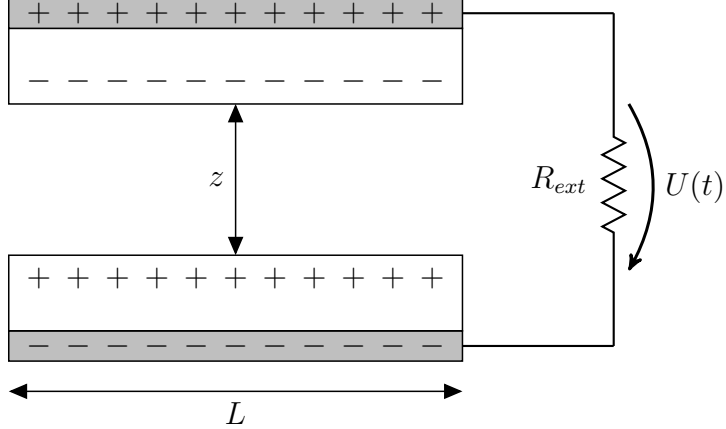


**Figure 2.2:** A typical contact mode harvester. Two dielectric (white) materials moving vertically making repeated contact when  $z = 0$  attached to an electrode (gray) on each side. The electrodes are connected through an external load  $R_{ext}$ .

Under open circuit conditions the induced voltage is calculated using

$$U_{OC} = \frac{\sigma z}{\varepsilon_0}, \quad (2.5)$$

where  $z$  is the separation gap [14]. Note how equation (2.5) is the exact same as calculating the voltage across an idealised parallel-plate capacitor.

To calculate the induced surface charge at short circuit conditions

$$Q_{SC} = \frac{WL\sigma z}{\delta + z}, \quad (2.6)$$

is used [14] with  $\delta$  from equation (2.2) and  $W$  is once again the width of the plates perpendicular to the paper.

The contact mode also acts as a capacitance similar to the sliding mode. However in this case the parallel-plate model with no extra assumption suffice as the plates are always fully overlapping. Thus

$$C_{teng} = \frac{\varepsilon_0 WL}{\delta + z} \quad (2.7)$$

## 2.2 Mechanical analysis

There are two main areas of mechanical analysis when simulating a TENG mounted to the inside of a tire. First one must find the deformation of the tire due to a multitude of factors in it's environment. This deformation in turn drives some response in the harvester which will elongate or compress accordingly.

### 2.2.1 Tire Deformation

For low modes of vibrations it is well established that a tire can be represented by the in-plane dynamics in a 2-dimensional slice of the tire [15, 16]. In this case low modes are defined as anything below 300 Hz. Using the conversions of table 2.1 it is clear that the deformations of interest, the one induced by the collisions against the ground are comfortable within these 300 Hz.

**Table 2.1:** Conversion between velocity-related units for calculations on a typical of radius  $R = 0.2532$  m. Another name for the frequency would be revolutions per second.

Linear velocity [km/h]	Angular velocity [rad/s]	Frequency [Hz]
10	10.97	1.75
20	21.94	3.49
50	54.85	8.73
100	109.71	17.46

When discussing this model it is important to establish names for a few important directions inside the plane. The radial direction refers to any vector pointing outwards from the hub perpendicular to its surface. The tangential direction refers to any vector which is tangential to the *radially deformed* tire carcass and the longitudinal direction is parallel to the ground. The azimuthal direction refers to any vector perpendicular to the radial direction and thus parallel with the surface of the non-deforming hub.

As is shown in figure 2.3, the hub and carcass of the planar model are connected by radial and azimuthal springs.

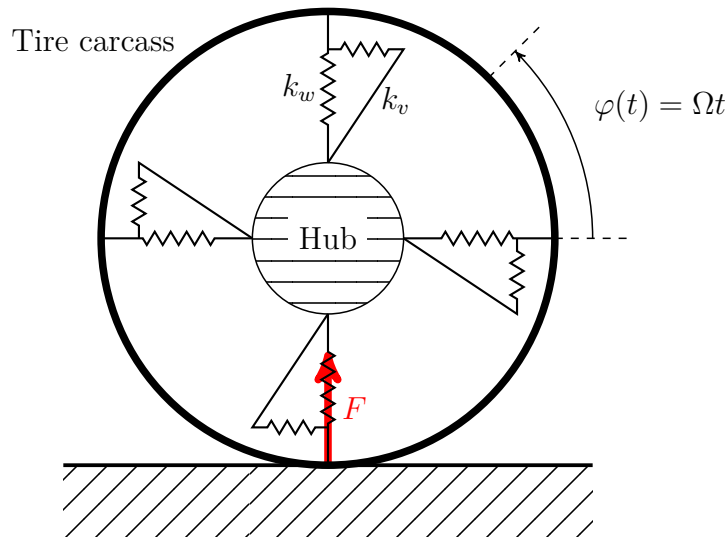


**Figure 2.3:** Planar tire model. The relative radii of the hub and tire carcass are **not** to scale.

The springs allow for radial deflection and shearing between the carcass and hub. Radial deflection of the tire carcass  $w$  is in most part derived from the normal force

## 2. Theory

---

$F$  acting as a response to the vertical load applied at the hub from the weight of the car.

To calculate the radial deflection numerically it is practical to use a modal expansion form [17]

$$w(\varphi) = \sum_{n=1}^N -nA_{n1}F_x \sin(n\varphi) + nA_{n2}F_z \cos(n\varphi), \quad (2.8)$$

where  $N$  is the maximal order of the expansion computed,  $A_{n1}$  and  $A_{n2}$  are *modal participation factors*,  $F_x$  is the external longitudinal force,  $F_z$  is the vertical external force and  $n$  is an order of the expansion form.

There are some simplifications to be applied before defining constituents of equation (2.8). Since the tire is assumed to be travelling at a constant speed  $F_x = 0$ . This eliminates half of the expression and with re-naming to a more terse notation the same equation is equivalent to

$$w(\varphi) = \sum_{n=1}^N n\lambda_n F \cos(n\varphi), \quad (2.9)$$

where  $\lambda_n = A_{n2}$  and  $F = F_z$  are the names to be used for the quantities henceforth.  $\lambda_n$  consists of many intermediate terms which will be defined before being combined into a useful expression, all of which are defined by [15].

When undergoing radial deformation the tire will also experience a tangential elongation as it is flattened against the ground. This is similarly calculated by

$$v(\varphi) = \sum_{n=1}^N -\lambda_n F \sin(n\varphi) \quad (2.10)$$

using the same definitions as equation (2.9) [17].

To model the complicated structure of a tire the model requires some material-, or rather tire-specific parameters presented in table 2.2.

Due to the tire rotating there exists a tensile force in the rubber due to centripetal acceleration (2.11)

$$\sigma_0 = p_0 b R + \rho A_{CS} R^2 \Omega^2. \quad (2.11)$$

Each modal order is subject to a modal equivalent mass (2.12)

$$m_n = \rho A_{CS} (1 + n^2), \quad (2.12)$$

it experiences a damping factor (2.13)

$$g_n = -4\rho A_{CS} n \Omega \quad (2.13)$$

and a stiffness factor (2.14)

$$k_n = \left( \frac{EI n^2}{R^4} + \frac{\sigma_0}{R^2} \right) (1 - n^2)^2 - p_0 b \frac{1 - n^2}{R} + k_v + k_w^2 n^2 - \rho A_{CS} (1 + n^2) \Omega^2. \quad (2.14)$$

**Table 2.2:** A list of physical parameters specific to the materials and constructions of a typical car tire.

Parameters	Unit	Description	Value
$b$	m	Carcass width	0.1600
$h$	m	Carcass thickness	0.0100
$A_{CS}$	$\text{m}^2$	Carcass cross-section area	0.0016
$\rho$	$\text{kg}/\text{m}^3$	Tire density	2280
$EI$	$\text{Nm}^2$	Carcass bending stiffness	1.41
$R$	m	Tire radius	0.285
$k_w$	$\text{Nm}^2$	Equivalent radial stiffness	$1.24 \cdot 10^5$
$k_v$	$\text{Nm}^2$	Equivalent tangential stiffness	$5.19 \cdot 10^5$
$p_0$	Pa	Inflation pressure	$3 \cdot 10^5$
$\Omega$	rad/s	Angular velocity	$\in [10, 110]$ (table 2.1)

With equations (2.11), (2.12), (2.13) and (2.14) we are ready for the definition of the modal participation factor (2.15)

$$\lambda_n = \frac{n}{\pi} \sqrt{m_n n^2 \Omega^2 + g_n n \Omega - k_n}. \quad (2.15)$$

Using equation (2.9) and (2.15) it now possible to obtain the (steady-state) radial deflection  $w$  at any angular position  $\varphi$  around the tire.

### 2.2.2 Harvester Response

Depending on mounting and/or construction of harvesters different displacements  $z(t)$  or  $x(t)$  will occur as a response to tire deformation. The response is independent of the triboelectric mode of the harvester in question. Each mode could be constructed to work in parallel or perpendicular to the tire surface.

First, consider a harvester mounted at two points some distance apart on the tire wall. Due to equation (2.10) it is known that these two points will oscillate along the tire wall. This motion could be harnessed in a sliding mode harvester, gliding along the tire wall but could also conceivably drive a contact mode harvester as well. The relative tangential movement of these two points located at angular coordinates  $\varphi_1$  and  $\varphi_2$  is simply described by the total elongation occurring between the two as described by equation (2.16)

$$x(t) = \int_{\varphi_1(t)}^{\varphi_2(t)} v(\varphi) d\varphi. \quad (2.16)$$

The response of harvesters working in the radial direction are in general not as well defined as their tangential counterparts. Usually one end of the harvester would be mounted against the tire wall, leaving the other end to move freely. In common for all radial harvesters are three forces working in this direction: the centripetal

## 2. Theory

---

normal force from resting against the tire wall, the (virtual) centrifugal force and gravity.

Since the angular coordinate  $\varphi$  is expressed in a non-rotating polar coordinate system a harvester mounted on the inside of a tire rotating at a constant angular velocity  $\Omega$  would have the position  $\varphi(t) = \Omega t$  as is expressed in figure 2.3. The centrifugal force  $F_C$  can be defined as

$$F_C(r, \varphi) = \begin{bmatrix} m\Omega^2 r \\ 0 \end{bmatrix} \quad (2.17)$$

where  $m$  is the mass of the harvester, the vector contains a radial (first) and a tangential (second) component. Gravity is defined as

$$F_G(r, \varphi) = \begin{bmatrix} -mg \sin(\varphi) \\ mg \cos(\varphi) \end{bmatrix} \quad (2.18)$$

where  $g = 9.81 \text{ m/s}^2$ .

The centripetal force is not modelled in the same manner as it is a reactive force, dependent on  $F_C, F_G$ , the (radial) position and velocity of the harvester. In simulations it is allowed to modify radial position and velocity directly, ensuring  $r \leq R - w(\varphi)$  at all times. On each time step where the harvester bottoms out, hitting the tire wall  $r$  is set to  $R - w(\varphi)$  and  $dr/dt = 0$ , simulating a fully inelastic collision. If the harvester is resting against the tire wall it inherits the velocity of the wall  $dw/dt$ .

Equations (2.17), (2.18) and the steps described in the paragraph above describe the harvester as a free, point like particle inside the elastic ring. This is the first model used to describe radial harvester response and is shown in figure 2.4.

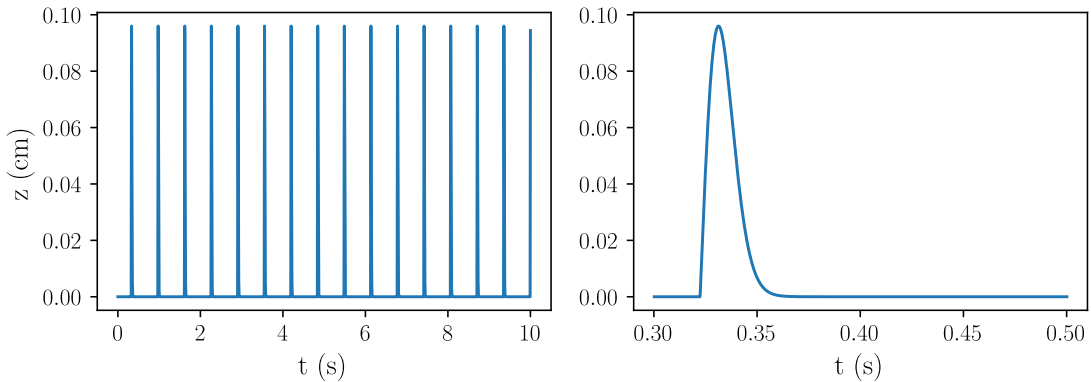


**Figure 2.4:** The free particle model. On the left is an example displacement series over time. On the right is a closer view of a single excitation. Note how the curve initially takes the form of a projectile motion until it meets the receding tire wall, dampening its fall.

The second model is a spring-mass subject to Hooke's law which introduces another

radial force in addition to the ones used in the free particle model

$$F_k(r, \varphi) = \begin{bmatrix} k(r_0 - r) \\ 0 \end{bmatrix} \quad (2.19)$$

where  $r_0$  is the equilibrium position of the spring and  $k$  is its spring constant. An example of this system is shown in figure 2.5.

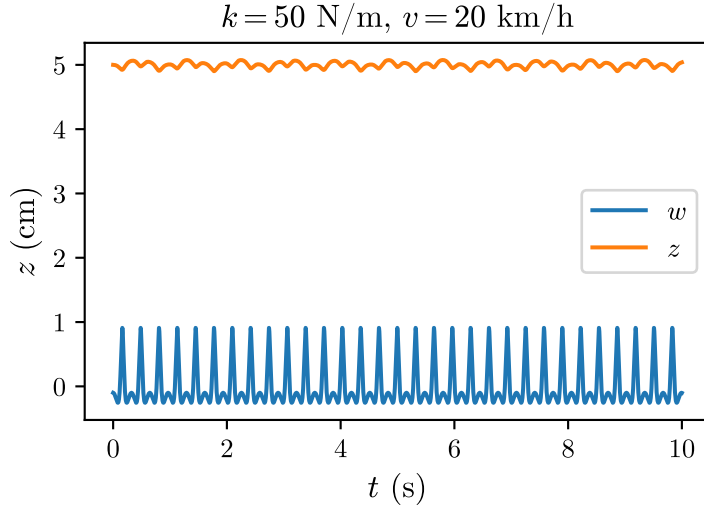


**Figure 2.5:** A spring-mass model for a vertical TENG. Shown in blue is the radial deflection  $w$  and in orange is the corresponding vertical harvester response  $z$ . This particular spring has  $r_0 = 5\text{ cm}$  and  $k = 50\text{ N/m}$ . Depending on how  $r_0$  and  $k$  are tuned, the spring can be made more or less responsive to the oscillations in  $w$ .

The third model isn't derived from any physical forces but is rather based on empirical observations. It has been observed that radial harvester responses are fast ( $< 0.1\text{ s}$ ) and of a roughly constant amplitude in its steady state [18]. Assuming that the shape of this fast displacement is unimportant, the displacement is defined as a piecewise linear pulse of an observed width and height, repeated at an observed frequency. An example of this model is shown in figure 2.6.

## 2.3 Circuit analysis

In contrast to the previous analysis in section 2.1, which focused solely on the phenomenon of charge generation, the following section examines the harvester as a lumped circuit element. Of particular interest is the scenario where a TENG is connected to an external purely resistive load  $R_{ext}$  since it describes many of the experiments conducted.

In the context of simulating a model, the avoidance of numerical instability is essential. To mitigate this risk, additional measures are undertaken to transform the model into a nondimensionalised form, thereby reducing the magnitudes of the

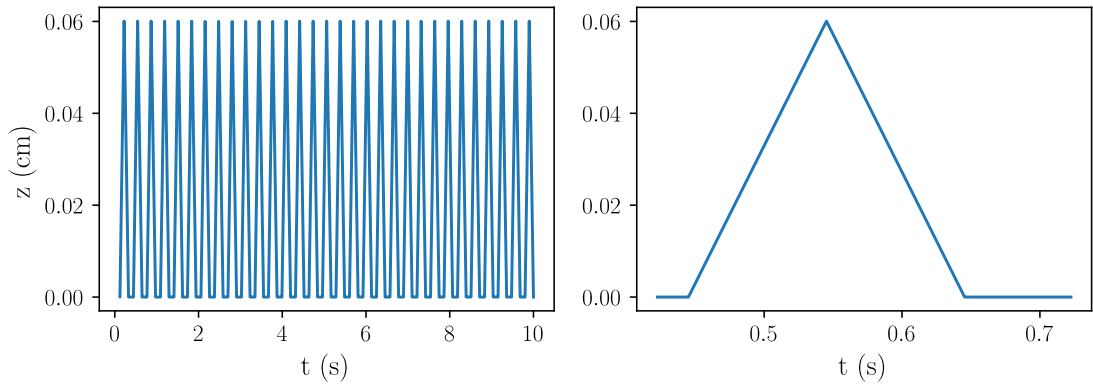


**Figure 2.6:** A series from the short pulse model of harvester response. Shown here is a relatively wide, but short pulse calculated for 20 km/h.

involved quantities towards zero. Through this process the susceptibility to computational errors or instability stemming from large or disparate numerical values is reduced.

It has been shown that a TENG can be modelled as a time dependent voltage source and a time dependent capacitance in series [19]. The entire circuit being analysed is shown in figure 2.7.

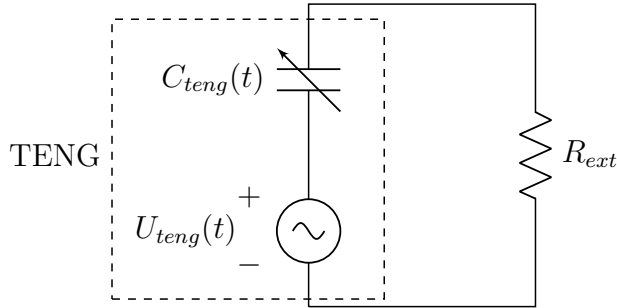


**Figure 2.7:** Equivalent lumped element circuit of TENG connected to a resistive external load. Note that both the capacitance and voltage are dependent on TENG displacement and thus time.

Central to the lumped circuit model is the so called  $V$ - $Q$ - $x$  (Voltage-Charge-Displacement) relationship. Outside the scope of this work, the relationship can be derived from Maxwell's equations which leads to

$$R_{ext} \frac{dQ(t)}{dt} = U_{OC} - \frac{Q(t)}{C_{teng}(t)} \quad (2.20)$$

where  $Q(t)$  refers to the amount of generated charges on each surface [5]. Assuming the initial condition  $Q(t = 0) = 0$  it is possible to solve equation (2.20) for the

charge

$$Q(t) = \exp\left(-\int_0^t (R_{ext}C(t'))^{-1} dt'\right) \cdot \int_0^t \frac{Q_{SC}(t')}{RC(t')} \cdot \exp\left(\int_0^{t'} (R_{ext}C(t''))^{-1} dt''\right) dt' \quad (2.21)$$

where  $Q_{SC}$  is chosen depending on the mode of the harvester in question [5].

Let

$$K(t) = \exp\left(\int_0^t (R_{ext}C(t'))^{-1} dt'\right) \quad (2.22)$$

which shortens equation (2.21) to

$$Q(t) = \frac{1}{K(t)} \int_0^t Q_{SC}(t') \frac{K(t')}{R_{ext}C(t')} dt'. \quad (2.23)$$

The remaining quantities of interest, namely induced current  $I$  and voltage  $U$  are obtained from the induced charge. Current is defined as the time derivative of charge and the voltage over  $R_{ext}$  is obtained through Ohm's law

$$I(t) = \frac{dQ}{dt}, \quad U(t) = R_{ext}I(t). \quad (2.24)$$

Likewise the power formula is employed to produce instantaneous power

$$P(t) = U(t)I(t). \quad (2.25)$$

As all quantities of interest have been found the process of nondimensionalising comes next. This has to be done separately for the sliding and contact mode due to the inherent differences in physical layout and governing equations.

In order to motivate the choice of nondimensionalising parameters with greater clarity the contact mode is presented before the sliding mode.

### 2.3.1 Nondimensionalising the contact mode

With the goal of nondimensionalising equation (2.23) in mind, the amount of surface charges  $q = \sigma WL$  is chosen as the characteristic charge to nondimensionalise the induced charges  $Q_{SC}$ . Using equation (2.6) one obtains

$$j = \frac{Q_{SC}}{q} = \frac{(\sigma WLz)/(\delta + z)}{\sigma WL} = \frac{z}{\delta + z}, \quad (2.26)$$

where  $j$  signifies the dimensionless charge. From here the displacement  $z$  can be non-dimensionalised using  $\delta$  as the characteristic length

$$f(t) = \frac{z(t)}{\delta}, \quad (2.27)$$

which in turn allows equation (2.26) to be written as

$$j(t) = \frac{f(t)}{1 + f(t)}. \quad (2.28)$$

Combining equation (2.7) and (2.27) yields

$$C_{teng}(t) = \frac{\varepsilon_0 WL}{\delta} \frac{1}{1 + f(t)}, \quad (2.29)$$

motivating a new nondimensionalising variable

$$A = \frac{\delta}{\varepsilon_0 R_{ext} WL}. \quad (2.30)$$

Using  $A$ , an intermediate function

$$G(t) = \int_0^t \frac{1}{AR_{ext} C_{teng}(t')} dt' = \int_0^t 1 + f(t') dt', \quad (2.31)$$

is introduced to aid in the nondimensionalising of  $K$ . Note how  $G$  only differs by a factor  $1/A$  from the exponent in equation (2.22). Thus

$$K(t) = \exp(AG(t)) \quad (2.32)$$

and in turn the induced charges can be nondimensionalised as

$$\begin{aligned} H(t) &= \frac{Q(t)}{q} = \frac{1}{K(t)} \int_0^t \frac{Q_{SC}(t')}{q} \frac{AK(t')}{AR_{ext} C_{teng}(t')} dt' \\ &= \frac{1}{K(t)} \int_0^t j(t) AK(t') (1 + f(t')) dt' \\ &= \frac{A}{K(t)} \int_0^t f(t) K(t') dt'. \end{aligned} \quad (2.33)$$

Note that the time  $t$  is left with the dimension of seconds and could be nondimensionalised using a characteristic time  $t_0$ , for example the period of  $z(t)$  derived from tire velocity. For numerical stability during the relevant simulations it does not matter, which is why it is neglected in this work.

Since the current over time is of interest, note that equation (2.24) implies

$$I(t) = \frac{dQ(t)}{dt} = \frac{d}{dt} (qH(t)). \quad (2.34)$$

For the purposes of simulations  $H$  can be numerically differentiated. Alternatively it is possible to show

$$I(t) = Aq [f(t) - (1 + f(t))H(t)] \quad (2.35)$$

for the contact mode [5].

### 2.3.2 Nondimensionalising the sliding mode

Any quantities not defined in the following derivation are defined in the same manner as in section 2.3.1. The expression for  $Q_{SC}(t)$  differs from the contact mode. Thus  $j$  has to be redefined

$$j(t) = \frac{Q_{SC}(t)}{q} = \frac{\sigma W x(t)}{\sigma WL} = \frac{x(t)}{L}, \quad (2.36)$$

where  $j$  signifies the dimensionless short-circuit charge. Again the displacement is nondimensionalised. However the length of each plate  $L$  is used as the characteristic length

$$f(t) = \frac{x(t)}{L}, \quad (2.37)$$

which in turn allows equation (2.36) to be written as

$$j(t) = f(t). \quad (2.38)$$

Using  $A$  from equation (2.30)  $G$  is defined as

$$G(t) = \int_0^t \frac{1}{AR_{ext}C_{teng}(t')} dt' = \int_0^t \frac{1}{1-f(t')} dt', \quad (2.39)$$

Thus  $K$  is still defined by equation (2.32) leading to

$$\begin{aligned} H(t) &= \frac{Q(t)}{q} = \frac{1}{K(t)} \int_0^t \frac{Q_{SC}(t')}{q} \frac{AK(t')}{AR_{ext}C(t')} dt' \\ &= \frac{1}{K(t)} \int_0^t j(t) \frac{AK(t')}{1-f(t')} dt' \\ &= \frac{A}{K(t)} \int_0^t \frac{f(t')}{1-f(t')} K(t') dt'. \end{aligned} \quad (2.40)$$

Once again  $H$  can be differentiated numerically or it is possible to use the analytical expression [5]

$$I(t) = \frac{f(t) - H(t)}{1-f(t)}. \quad (2.41)$$

## 2. Theory

---

# 3

## Methods

The methodology was planned with short and frequent iteration cycles in mind. Since the efficacy of contact electrification and it's implementation in tires are largely unknown it was important to attempt multiple solutions both in simulation and experiments.

Simulations were interspersed with physical experiments at RISE laboratories in Gothenburg, Sweden and at Nokian Tyres testing facility in Nokia, Finland. The simulations were intended to guide the physical experiments to give an idea of what parameters to vary and mounting options for different types of harvesters.

Experiments in turn functioned as confirmation or rejection of simulated phenomena to further correlate simulations with reality.

### 3.1 Simulations

A model based on the three theoretical aspects presented in chapter 2 was constructed using the *Rust* programming language [20]. The language was chosen since it strikes a good balance between runtime performance, development velocity and long term maintainability for the purposes of numerical simulations.

Mechanical and electrical phenomena are developed in a modular fashion to not only allow for end-to-end simulations but also electrical simulations from displacements not derived from tire deformations such as experimental data.

#### 3.1.1 Mechanical simulations

Using equations (2.9) and (2.10) the tire displacement can be sampled at any arbitrary angle  $\varphi$ . A tire rotating with the constant angular velocity  $\Omega$  produces a time series  $z(t) = w(\Omega t)$ .

However it is practical to convert the polar  $r, \varphi$  coordinate system to a Cartesian  $z, x$ . Thus the tire is unwrapped and the new coordinate system is introduced to a virtual (and vertical) centrifugal force in addition to a rotating gravitational force.

Initial conditions are a constant angular velocity  $\Omega$ , no acceleration  $\varphi = 0$  as per figure 2.3.

The parameters were selected according to table 2.2. Note that the values for  $k_v$  and  $k_w$  are unknown for the tires utilized in the physical experiments. Despite this, any potential differences to values used in other studies [15, 17] are deemed insignificant, given that the simulations primarily aim to offer qualitative insights into trends and potential phenomena, rather than providing precise quantitative results for specific experimental configurations.

#### 3.1.2 Electrical simulations

Since the differential equations describing the electrical system have already been solved analytically the resulting integral can be integrated numerically. The time integral of equation (2.23) is solved with nested usage of the trapezoidal rule on discrete intervals of time at varying densities. Time steps are generally chosen with respect to the numerical stability of the solution.

One important consideration is the convergence of  $K(t)$ . Since  $R_{ext}, C(t) \geq 0$ ,  $K(t)$  is monotonically increasing. Precision deteriorates when using 64-bit floating point numbers of increasing magnitudes which puts an upper bound on  $t$  after which the numerical integration of  $K(t)$  can no longer be trusted.

As previously mentioned the electrical simulation is completely decoupled from the mechanical simulation of the tire and harvester response. As such it can be run over any arbitrary time series of harvester displacement which is leveraged to confirm a correct implementation in accordance with figures presented in prior works within the field [5].

## 3.2 Physical experiments

A primary goal of the physical experiments was to verify simulated data. In particular correlation between qualitative predictions made from simulations to confirm or reject the validity of said calculations.

Additionally these experiments serve the unique purpose of quantitative analysis, allowing some insight into the produced amount of current and voltage under controlled circumstances. They also give unique insight into energy losses and degradation of TENGs.

#### 3.2.1 Experiments at RISE

Many version of sliding and contact mode TENGs were constructed in attempts to quantify electrical properties for each design. At first each version had to be displaced manually but later on an automatic device was constructed which allowed for more consistent motion.

All measurements at RISE were conducted in the electric lab. A *Rohde & Schwartz RTB2004* [21] oscilloscope was used to measure voltages with an accompanying probe.

### 3.2.1.1 TENG voltage

A simple contact mode harvester was built from copper tape and Kapton mounted onto a folded sheet of PP (polypropylene) [22] to act as a sprung base for oscillations. It's voltage was measured using  $1\text{ G}\Omega$  of input impedance to get as close to the open-circuit voltage as possible.

A harvester using the same design could be cut at the folded ends into two separate planes. These are then slid against each other horizontally as opposed to the previous vertical movement to form a sliding mode harvester. It's open-circuit voltage was then measured in the same manner.

### 3.2.1.2 Robotic actuation

To provide consistent displacement a continually rotating servo was used to displace the harvesters during further experiments. The servo, controlled by an Arduino Uno [23] rotates a wheel equipped with cams. Each cam in turn pushes an arm which compresses an attached harvester. After reaching the end of a cam the arm is returned to it's original position using a spring. A schematic of the construction can be seen in figure 3.1. A modified arm can be used to attach a sliding mode harvester.

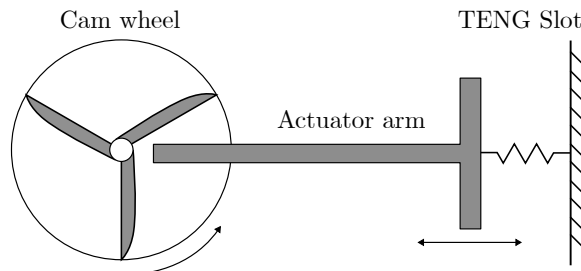


**Figure 3.1:** A schematic figure of the robotic actuator.

Several arms of different lengths were produced to control the amplitude of the motion while frequency was modulated by the PWM port on the controller board. As the Arduino was incapable of providing sufficient power for running the servo at maximum speed it was only used for it's pulse width modulation capabilities. Power was instead supplied through a modified USB-cable connected to a wall socket via a commercial 5-volt DC phone adapter.

In general the robotic actuator was used at a frequency of 2.1 Hz when measuring all harvesters. The amplitude was set to 12 mm for contact mode harvesters and to 6 mm for sliding mode to resemble prior observations in tires [24].

### 3.2.1.3 TENG current

A harvester was mounted in the robotic actuator, it's output connected to a full wave rectifier which in turn charges a capacitor. Measuring the voltage over this capacitor using an oscilloscope gives the contained charge by

$$C = \frac{Q}{U}, \quad \frac{dQ(t)}{dt} = I(t) \iff I(t) \approx \frac{C\Delta U}{\Delta t}, \quad (3.1)$$

since the capacitance is known.

### 3.2.1.4 TENG capacitance

As the TENG is computationally modelled in part as a time-dependent capacitor it's capacitance was measured at varying displacements using a LCR-bridge. Each end of the harvester was attached to a vise which allowed for sub-millimeter precision control of the displacement. However the vise itself might interfere when measuring the small capacitance. To combat this risk large plastic boxes were attached to each of the vise which the harvester parts in turn are attached to. This separates the harvester from the cast iron vise and removes any potential influence.

### 3.2.1.5 Reverse taping

This is a simple measurement where two attached electrode sliding mode harvesters of copper and Kapton are constructed. The only difference between them being how the copper tape is attached.

On the first, the copper is taped to the exterior sheet of PP with the Kapton sheet wrapped tightly over the copper tape. On the second the copper is instead taped onto the Kapton, with both subsequently glued onto the exterior PP sheet. The former is referred to as conventional taping while the latter is referred to as reverse taping.

### 3.2.1.6 Grated sliding TENG

An idea arose to enhance a sliding mode harvester by a geometric layout inspired by flexible printed circuit [25]. Since  $U_{OC}$  depends inversely on  $(L - x)$  according to equation (2.1) it is clear that maximising the amplitude of the sliding motion would lead to increased energy production.

On the other hand  $L$  could instead be minimised to produce the same results. Theoretically this would not reduce the voltage or induced charge as long as  $x < \leq L$ . Thus a comb-like layout was constructed to provide a smaller length  $L$  in the sliding direction while maintaining a surface area on the same order of magnitude.

Voltage and current was measured for the grated sliding harvester and a simple harvester built of the same materials and footprint (external dimensions). Simple, in this case refers to a rectangular harvester with no additional geometric constructions.

### 3.2.1.7 Sliding direction

To better understand the dependence on  $(L - x)$  of equation (2.1) measurements were carried out using rectangular harvesters, sliding them using the robotic actuator along their longer and shorter sides.

A square harvester using copper electrodes and Kapton as the dielectric was constructed with an initial width and length of 50 mm. It was measured sliding along its width and length (which at this point is arbitrary due to its square shape). Then the harvester was cut down to a width of 37.5, 25 and 12.5 mm, measuring its output current and voltage along both directions between each modification.

### 3.2.1.8 Material selection

At RISE there was access to a selection of electrode and dielectric materials for harvester construction. The available electrodes were

- Copper tape
- Aluminium tape

The available dielectric films (and their respective thicknesses) were

- Kapton (25  $\mu\text{m}$ ) [26]
- Kapton (75  $\mu\text{m}$ ) [27]
- FEP (25  $\mu\text{m}$ ) [28]
- FEP (127  $\mu\text{m}$ ) [29]
- Tekfilm (25  $\mu\text{m}$ )
- PEEK (25  $\mu\text{m}$ ) [30]
- Mylar (25  $\mu\text{m}$ ) [31]

Every electrode was tested using every dielectric film, resulting in 14 harvesters measured for produced current and voltage.

## 3.2.2 Experiments at Nokian Tyres

There exists a tyre testing machine at Nokian Tyres facilities in Nokia, Finland which was allowed to be borrowed during this project. A schematic figure of the testing rig is shown in figure 3.2. It consists of a large spinning drum acting as the ground and an arm onto which a tyre is mounted to roll it against the artificial ground. The arm can move to adjust the load applied to the tire while the drum

### 3. Methods

---

can change in angular velocity.

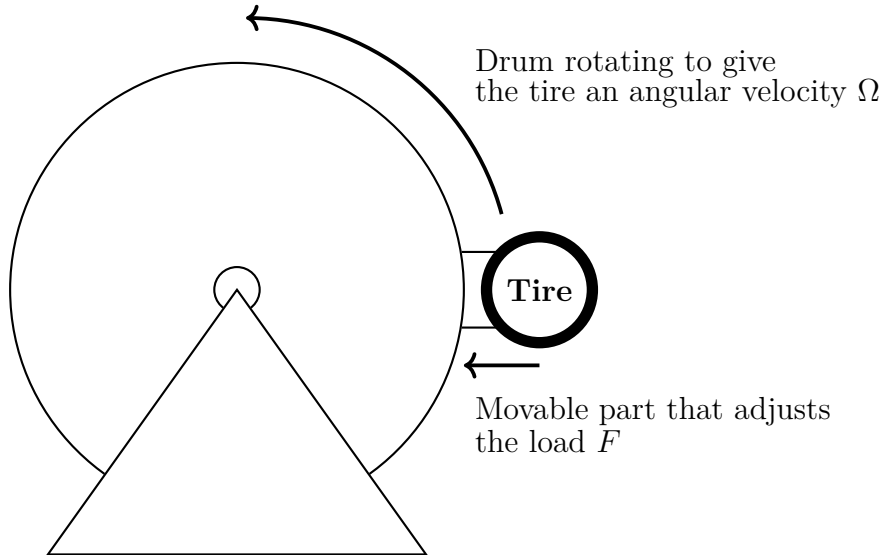


**Figure 3.2:** A schematic of the tire testing rig. The tire is fastened using a reusable testing rim. For each adjustment of the TENG or circuitry, the rim is removed from the rig before the tire can be separated from the rim, allowing access to its internals.

This setup provided invaluable measurement opportunities due to the harsh environment and access to forces which could not be reproduced in the lab. Most important of these are the centrifugal forces and impact forces which occur each time the harvester rolls into the tire's contact patch, hitting the ground.

Four modified contact mode harvesters shown in figure ??? and two grated sliding TENGs were brought for trials inside tires under applicable working speeds for a car during regular use. A double-sided tape was used to attach the harvesters onto the inside of the tire wall. Measurements were conducted for each harvester to determine output voltage and current under varying loads and speeds.

A measurement circuit combined with a Bluetooth transmitter provided by RISE was mounted together with the harvesters to wirelessly send data to a computer for further processing and analysis.

#### 3.2.2.1 Modified contact mode TENG

A novel mounting for the contact mode harvester was implemented to overcome the centrifugal force. Each end of the construction is mounted to the tire wall using double-sided tape. The tangential stretch of the tire wall pulls/pushes on the film, closing/opening it periodically.

The two copper electrodes are connected to the Bluetooth measurement unit which allowed for wireless data transfer in real time during the measurement runs.

The harvester was measured, charging a capacitor under a 1500 N load at 10 and

20 km/h. Its output voltage was then measured under the same load at speeds of 30, 50, 70, 90 and 110 km/h.

### 3.2.2.2 Grated sliding mode TENG

Two harvesters of the same grated sliding mode design used in the experiments of section 3.2.1.6 was brought to Nokia. The slider was attached to a 20 cm long PP (polypropylene) film to maximise the oscillation amplitude. To prevent the accumulation of rubber and dirt an antistatic bag was mounted around region where the slider overlaps the electrodes.

The harvesters were measured charging a capacitor under a 1500 N load at 10 and 20 km/h. Their output voltage was measured under loads of 1500 and 3000 N at speeds of 10, 20 and 30 km/h. The speed was kept low in order to protect the measurement electronics since these measurements where made prior to the modified contact mode measurements.

### 3. Methods

---

# 4

## Results

Due to leveraging both simulations and physical experiments at multiple physical locations there are a multitude of figures and tables that have been accumulated over time. Generally these are presented in chronological order although there are some breaks in the order for the sake of clarity.

Many of the experiments were conducted multiple times to account for information gained during later experimentation. In general these first attempts have been omitted due to them acting in large part as learning experiences rather than producing data of any value.

An important metric to keep in mind while pondering the physical experiments is the root-mean-squared power. For the purposes of acting as a power source to wireless sensors, the harvesters would need to produce a RMS-power in the mW range.

### 4.1 Simulations

Significant effort was spent to improve the runtime performance of simulations during the project. Eventually this allowed for computations previously considered impossible such as parameter sweeps over area, external resistances and so on.

This increase in computational efficiency lead to some later simulations making earlier ones obsolete. Regardless, the early simulations are presented here to provide context for the evolution of the software.

### 4.1.1 Mechanical simulations

Using the parameters of table 2.2, a radial and tangential displacement was calculated for every angle  $\varphi$  which is shown in figure 4.1.

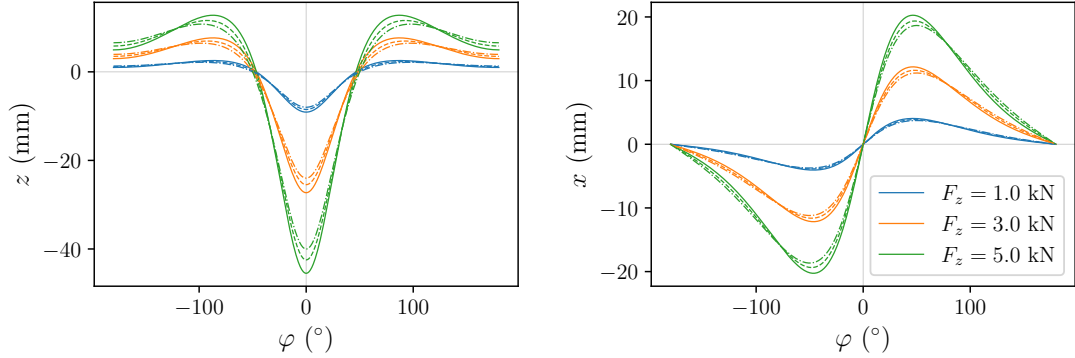


**Figure 4.1:** The plot shows how radial and tangential displacement varies with azimuthal angle for different vertical loads. Each color represents a specific vertical load ( $F_z$ ). Line styles indicate different pressures: solid lines for 220 kPa, dashed lines for 260 kPa, and dash-dotted lines for 300 kPa.

Note the different definitions of azimuthal and tangential. Azimuthal refers to the direction perpendicular to the radial direction in the tire plane. Tangential on the other hand refers to the direction tangential to the tire surface at any azimuthal coordinate  $\varphi$ .

The results of figures 4.1 can be expressed in polar coordinates to show the effects on a circular tire which is shown in figure 4.2.

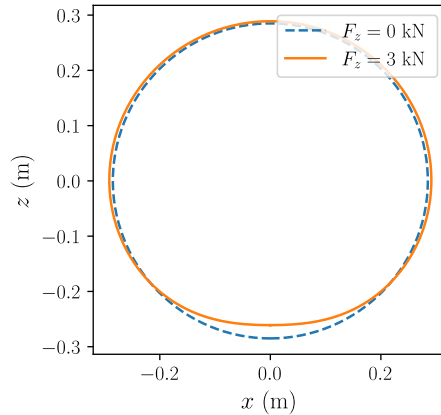


**Figure 4.2:** A displaced tire (orange/solid) compared to it's unstressed (blue/-dashed), circular initial shape. Note that the tangential displacement occurs along deformed tire shape and as such is not clearly visible when plotted in this manner.

These displacements were used to calculate harvester actuation series with the spring-mass and free particle models described in section 2.2. As it turned out, both models failed to provide actuation in line with experimental results.

Examining a spring-mass system inside the tire at different velocities shows complete capitulation to the centrifugal force for any velocities above walking speeds. An example of this is shown in figure 4.3. The centrifugal force could of course be counteracted by a stiffer spring, however this leads to other phenomena absent in experimental data such as resonance phenomena and overtones among others.

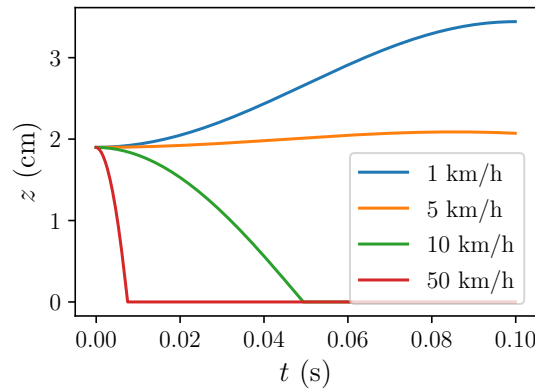


**Figure 4.3:** Spring height over time for increasing velocities. Note how the spring height collapses to 0 for speeds at 10 km/h and above.

The free particle model similarly surrenders to the centrifugal force, leaving the particle forced against the tire wall at all times. To illustrate why this occurs at all velocities a diagram showing the imagined path of a particle if it were allowed to fall through the tire wall is presented in figure 4.4.

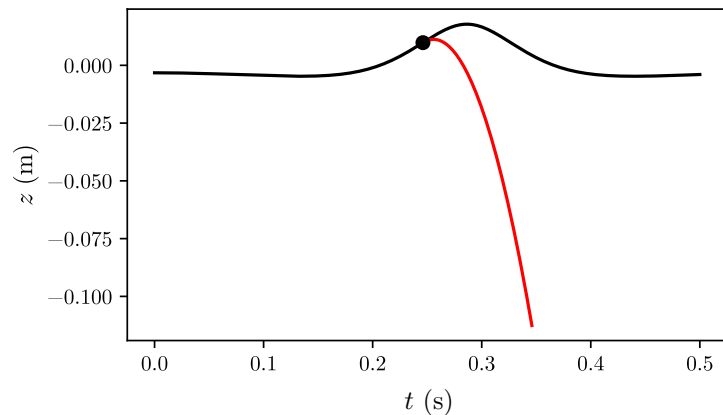


**Figure 4.4:** Harvester actuation over time shown in black. Highlighted with a dot is the inflection point of the actuation curve. Shown in red is the trajectory of a free particle falling from the inflection point under the associated centrifugal force.

No matter the tire velocity, a particle resting against its wall will never receive a

## 4. Results

---

sufficient launch velocity to overcome the rest of the tire deformation ahead of it during a revolution.

When mounting a sliding mode harvester on a tire the two parts sliding over each other are fastened at two separate points. The relative motion of the two mounting points  $\varphi_1$  and  $\varphi_2$  is described by equation (2.16).  $x(t)$  is calculated for an entire revolution, noting the maximum value. Figure 4.5 shows these maximal actuation values for increasing mounting point separation  $r(\varphi_2 - \varphi_1)$ .

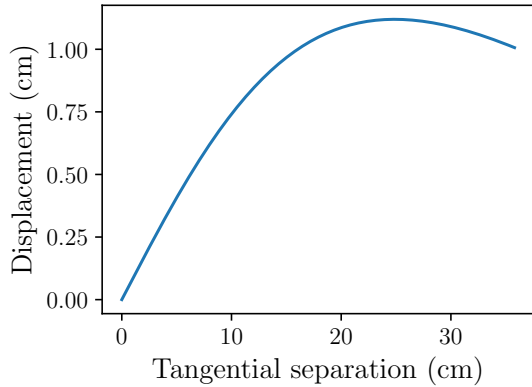


**Figure 4.5:** The maximum tangential displacement obtained during a tire revolution for increasingly separated mounting points.

### 4.1.2 Electrical simulations

Under an oscillating harvester actuation the induced current and voltage undergo a transient charging phase before settling into a steady state solution. One such example is presented in figure 4.6. In addition to inducing current the harvester also produces a negligible force in reaction to actuation which is presented here but in general is not considered in other calculations.

An important consideration when integrating a TENG into an external circuit is its output impedance. There exists some optimal  $R_{ext}$  for which the harvester produces the maximum output power. Repeated 10 s simulation runs with increasing values of  $R_{ext}$  were used to calculate the maximum current, voltage and power with the addition of mean power which are then plotted against  $R_{ext}$  in figure 4.7.

A phenomena predicted by simulations is a saturation of power output as tire speeds increase. Running simulations of identical parameters, only varying the tire velocity indicates a power saturation as the velocity increases. One instance of this is shown in figure 4.8. When varying the area of simulated harvesters it is evident that saturation occurs at lower speeds for larger harvester areas. It is even possible for power output to decrease at higher velocities using sufficiently large harvesters.

For clarity's sake it is important to note that saturation occurs for every attempted oscillating actuation series where the length of an excitation depends on the fre-

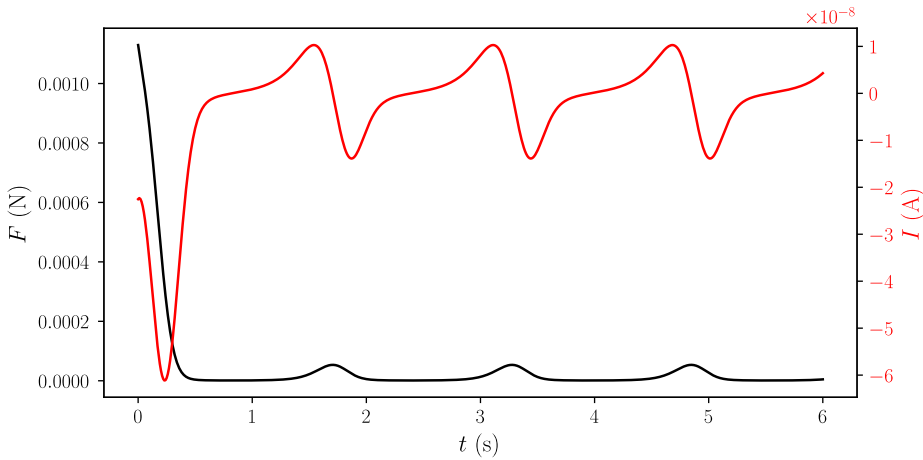


**Figure 4.6:** Induced current (red) and reactive force (black) of a contact mode harvester subject to an oscillation actuation.

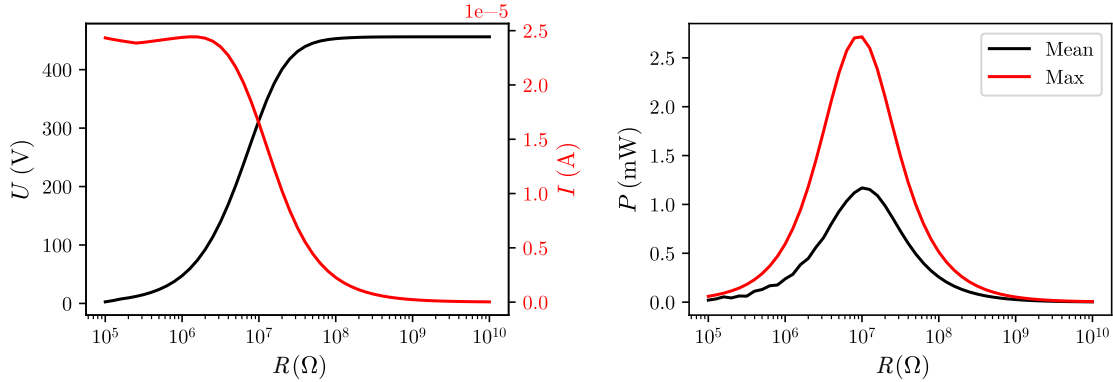


**Figure 4.7:** Shown on the left is voltage (black) and current (red) over a range of  $R_{ext}$ . On the right is the mean (black) and maximum (red) power recorded during the same simulations.

quency of the oscillation. It is independent of the mechanical simulation from which harvester actuation can be derived.

Both the length and width of a sliding mode harvester are of particular interest when optimising a TENG design. They are the only continuous parameters which can be easily adjusted during physical experiments when constructing harvester. Understanding their impact on performance is therefore of great interest. In figure 4.9 a heat map is shown, depicting the root-mean-squared power,  $P_{RMS}$  of a sliding mode harvester undergoing a periodic oscillation with  $f = 2$  Hz and an amplitude of 6 mm.

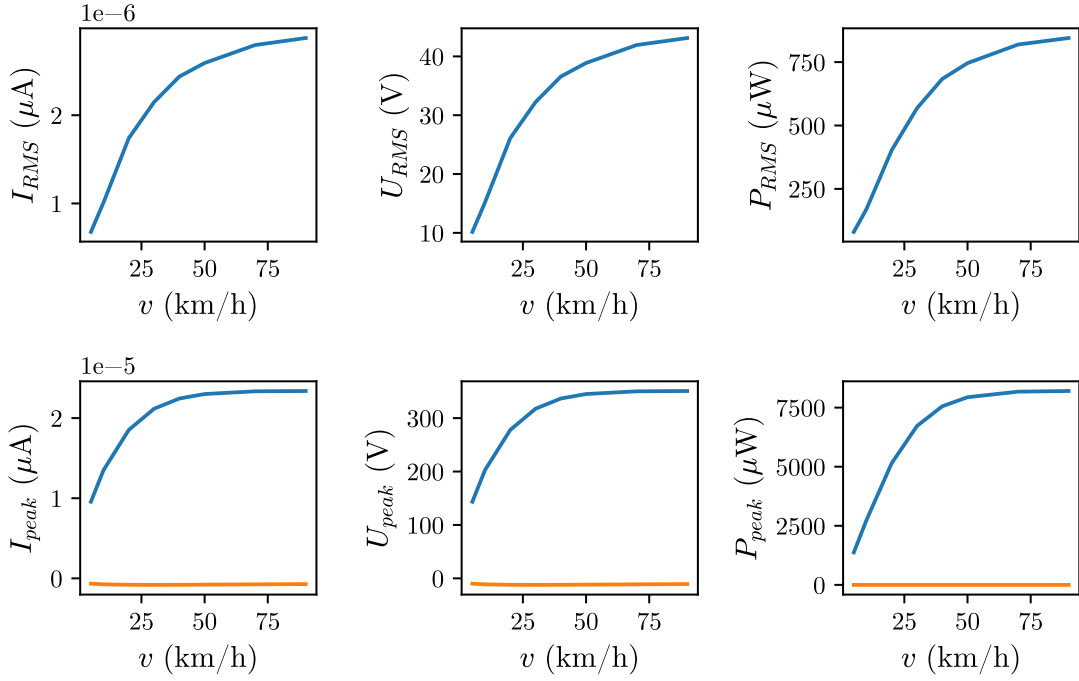


**Figure 4.8:** Peak and root-mean-squared values for current, voltage and power. For the peak curves, blue indicates the positive peaks with orange signifying the negative peaks (which are trivially 0 for power).

## 4.2 Physical experiments

The physical experiments encompassed a range of analyses conducted both at RISE and Nokian Tyres, focusing on voltage, current, and capacitance measurements across various energy harvesters. Detailed descriptions of the outcomes are outlined in the respective sections. These experiments provided insights into the performance, efficiency, and potential applications of various TENG constructions.

### 4.2.1 Experiments at RISE

The process of measuring voltage and current was carried out during most of the experiments discussed below. For detailed descriptions see sections 4.2.1.1 and 4.2.1.3. In general voltage was measured with  $1\text{ G}\Omega$  resistance on the oscilloscope probe. Currents are generally measured over a  $100\text{ nF}$  or  $180\text{ nF}$  capacitor using  $1\text{ M}\Omega$  probe resistance.

#### 4.2.1.1 TENG voltage

The first harvester built during experiments at RISE was a  $30 \times 30\text{ mm}$  single-electrode contact mode harvester. A picture of the harvester is shown in figure 4.10. The folded outer layer of PP acts as a spring to ensure separation when no load is present. The electrode is made out of kitchen aluminium foil, glued onto the PP with a wire

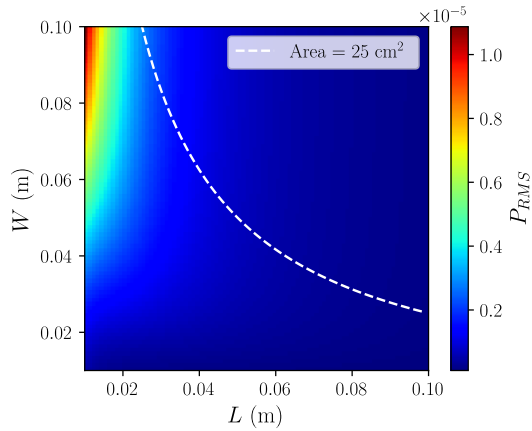


**Figure 4.9:**  $P_{RMS}$  for different values of  $W$  and  $L$  from 1 cm to 10 cm. A level curve of area at  $W \cdot L = 0.025 \text{ cm}^2$  is highlighted with a dashed line. Note how a large  $W$  combined with a small  $L$  provides the maximum power output.

between the two to act as an output terminal. A sheet of  $25 \mu\text{m}$  thick Kapton is glued over half the electrode to act as an electron donor for contact electrification.



**Figure 4.10:** An initial harvester prototype used to demonstrate contact electrification.

The single electrode was measured against the ground of an oscilloscope using a  $1 \text{ G}\Omega$  voltage divider. The measurement shown in figure 4.11 presents confirmation of contact electrification, although producing a low voltage.

#### 4.2.1.2 Robotic actuation

Due to changes in harvester dimensions during the project and the addition of sliding mode harvesters, the design underwent some manual alteration such as grinding with sandpaper and files. The final design itself can be seen in figure 4.12.

A measurement was conducted to determine an estimate for the actuators tolerances. Using a script to find each peak-to-peak voltage in a time series, the standard

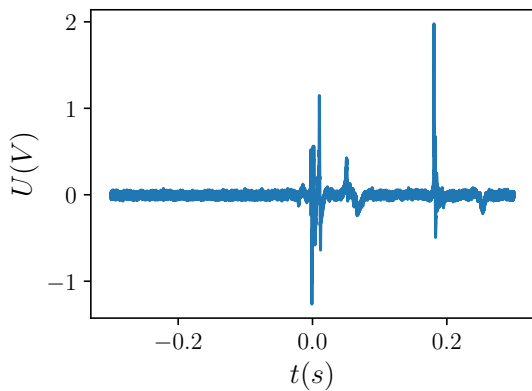


**Figure 4.11:** Output single electrode voltage for the first harvester prototype. The harvester is left passive, without actuation during  $t < 0$  before being manually displaced during  $t \geq 0$ .

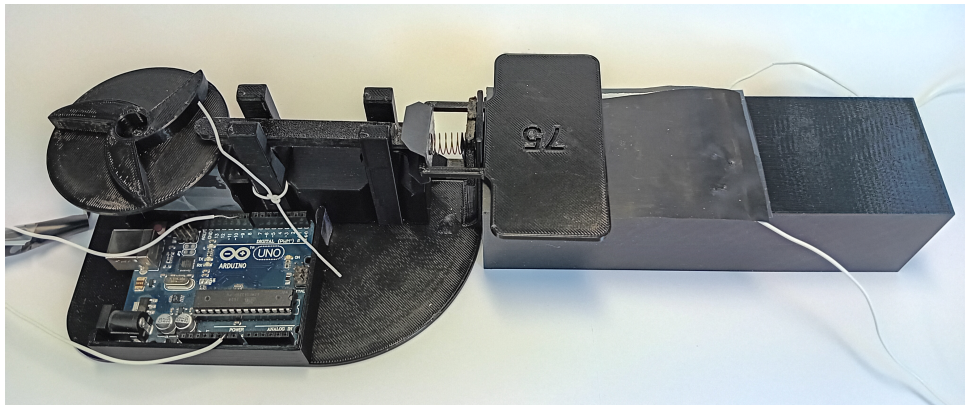


**Figure 4.12:** The final 3D-printed robotic actuator.

deviation of the voltage can be used as a measurement of actuation consistency. The results of this calculation are presented in figure 4.13.

#### 4.2.1.3 TENG current

Generally the TENGs constructed during most experiments were measured to output currents in the range 100-200 nA. To be able to apply equation (3.1), a low pass filter is applied to the signal before the last drop in voltage is linearised providing  $I(t)$ .

An example of this process is shown in figure 4.14 which was the best performing harvester measured during the entire project. It was constructed using electrodes of aluminium tape, 127  $\mu\text{m}$  thick FEP as a dielectric, all cut to 90  $\times$  50 mm. The TENG was actuated using the robotic actuator at 2 Hz with an amplitude of 6 mm in the longitudinal direction.

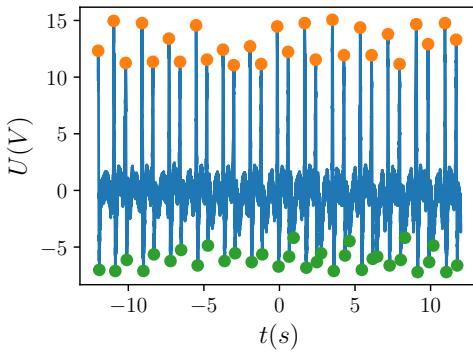


**Figure 4.13:** Data used to calculate the standard deviation of  $U_{PP}$ . Detected maxima are shown in orange, minima in green. Each successive maxima and minima are subtracted, forming a series of voltages, the standard deviation of which is 0.86 V at a mean  $U_{PP}$  of 19.0 V.

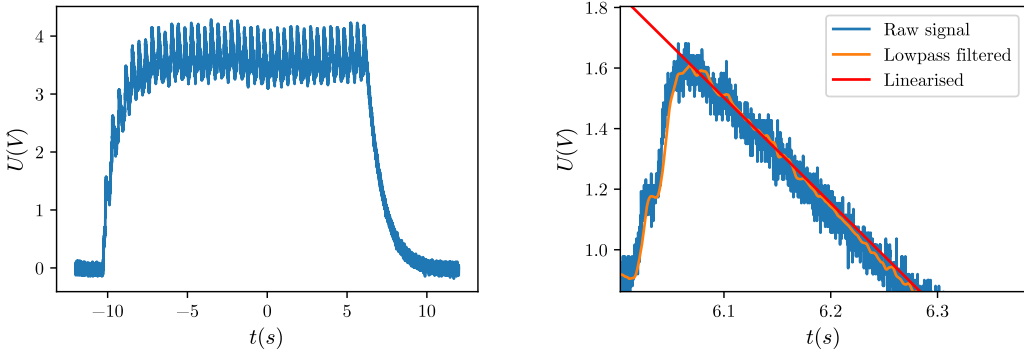


**Figure 4.14:** Shown on the left is the entire measurement from charging the capacitor to its discharge. On the right is an enlarged view of the final peak of the measurement signal in its original form, filtered and a linear approximation of the discharge. The resulting current is 375 nA.

#### 4.2.1.4 TENG capacitance

Capacitance was measured for sliding and contact mode harvesters, attempting to verify equations (2.4) and (2.7).

When measuring the sliding mode, two measurements were conducted on the same 50×25 mm harvester. Once sliding it open along its long side, once along its short side which is shown in figure 4.15. When curve fitting against the measured data, the only parameter left to be fitted for the sliding mode is  $\delta$ . For the 50 mm edge  $\delta = 0.00027$  m and for the 25 mm edge  $\delta = 0.000208$  m.

Since the contact mode operates orthogonally to the surfaces in question there's no point in rotating the harvester as there's only one unique measurement series to make. Curve fitting against equation (2.7) for  $\delta$  didn't suffice to produce anything

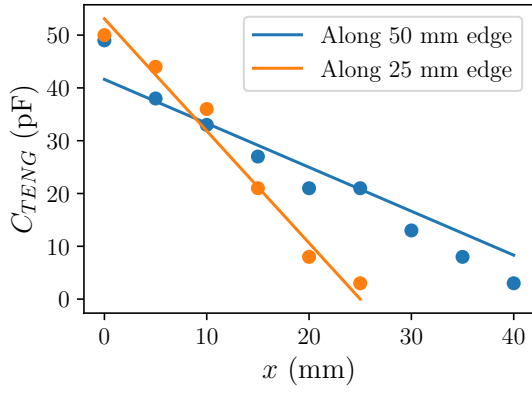


**Figure 4.15:** Measured (points) and curve fit (solid lines) capacitance for a sliding mode harvester along it's two directions.

resembling the measured data. If allowed to fit for the area  $W \cdot L$ , it is possible to match the measurements as is shown in figure 4.16. However, the harvester in question has an area of  $0.0032 \text{ m}^2$  whereas curve fitting gives  $\delta = 0.00043 \text{ m}$  and  $W \cdot L = 0.34 \text{ m}^2$ .

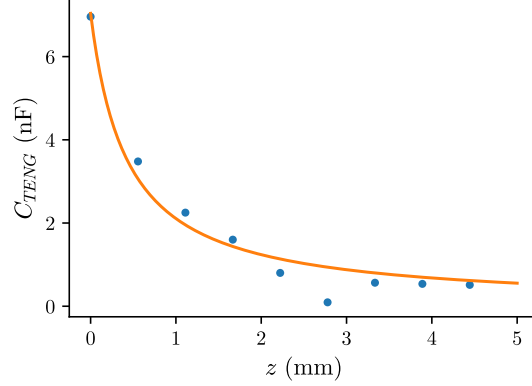


**Figure 4.16:** Measured (points) and curve fit (solid lines) capacitance for a contact mode harvester over vertical separation.

#### 4.2.1.5 Reverse taping

Measuring the output current and voltage for both harvester variants gave the results presented in table 4.1. Taping the electrode onto the Kapton film results in a thinner harvester and prevents crinkles from forming on the dielectric film during sliding mode actuation.

**Table 4.1:** Output current and voltage for two methods of taping copper electrodes.

Variant	Current (nA)	Voltage (V)
Conventional taping	74.5	76.4
Reverse taping	105	32.2

#### 4.2.1.6 Grated sliding TENG

Measuring the performance of the grated sliding TENG against a simple TENG built from the same copper tape and  $25\ \mu\text{m}$  Kapton film showed a significantly higher power output for the simple design. The measurements shown in figure 4.17 indicate currents of  $7.23\ \text{nA}$  and  $23.9\ \text{nA}$  for the grated and simple harvesters respectively.  $U_{PP}$  for the grated harvester was  $5.84\ \text{V}$  compared to  $56.4\ \text{V}$  for the simple design.

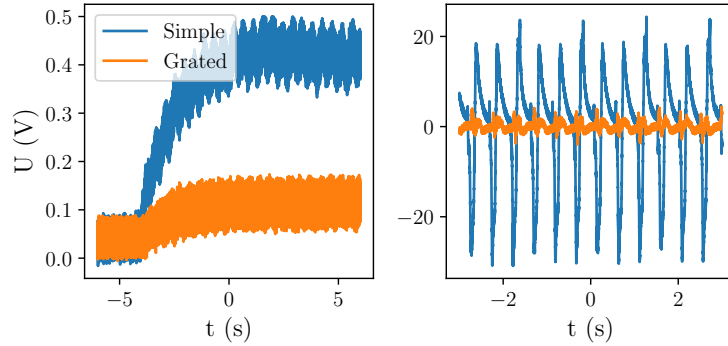


**Figure 4.17:** On the left is the voltage across the  $178\ \text{nF}$  being charged. On the right is the output voltage of each harvester across a  $1\ \text{G}\Omega$ . Note the superior performance of the simple harvester in both graphs.

#### 4.2.1.7 Sliding direction

With a reverse taped copper-Kapton sliding mode TENG, initially  $50 \times 50\ \text{mm}$  in size, the relationship between longitudinal and transverse performance is measured which is shown in figure 4.18. At each step in the process, current and voltage are measured along both directions before cutting the harvester down to a smaller size.

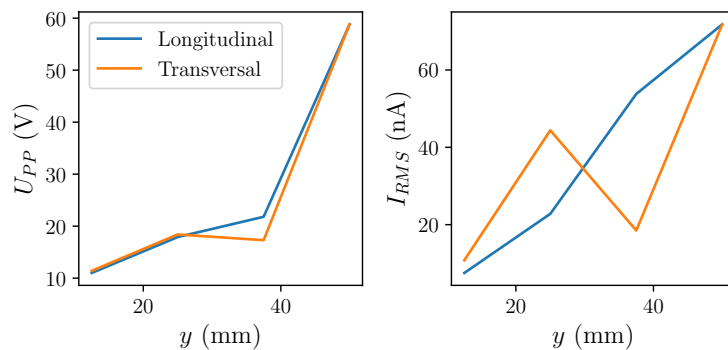


**Figure 4.18:** Output voltage and current for a harvester actuated along the longitudinal and transverse directions.

As the harvester is reduced in width by increments of  $12.5\ \text{mm}$ , the output current and voltage decreases in similar quantities for both orientations.

#### 4.2.1.8 Material selection

Two pairs of  $50 \times 50$  mm electrodes were manufactured from copper and aluminium tape. Each dielectric film was in turn tightened over one of the electrodes using tape to build each harvester. Voltage was measured over a  $1\text{ G}\Omega$  resistor and current was measured by charging a  $178\text{ nF}$  capacitor in the same manner as during section 4.2.1.6. The results of these measurements are presented in figure 4.19.

Generally the usage of aluminium electrodes results in higher currents while the effect on voltage seems to be dependent on the particular dielectric in question. However for the best performing dielectrics, Kapton and FEP, both  $25\text{ }\mu\text{m}$  thick the aluminium electrodes lead to increases in both current and voltage.

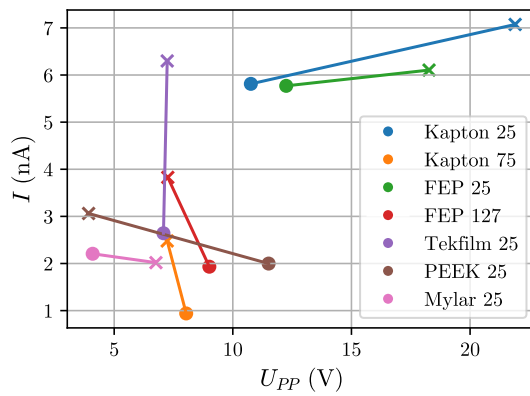


**Figure 4.19:** Current and voltage measured for each electrode-dielectric combination. Dots indicated the usage of copper electrodes and crosses signify aluminium electrodes.

### 4.2.2 Experiments at Nokian Tyres

The measurements in Nokia primarily focused on confirming tendencies observed in the lab and simulations. The harvesters proved more durable than anticipated, never breaking during any of the tests. However a measurement circuit broke during a test at 110 km/h under 1500 N load.

#### 4.2.2.1 Modified contact mode TENG

The resulting construction is shown in figure 4.20. Both electrodes consist of copper tape fixed onto an outer layer of PP. One is covered by a sheet of 25  $\mu\text{m}$  thick Kapton.



**Figure 4.20:** The modified contact mode TENG tested at Nokian Tyres. On the left is the complete design and on the right is the same harvester cut open to show both electrodes.

When measuring the modified contact mode TENG for a series of velocities which is shown in figure 4.21, an initially promising voltage output is shown to tend towards zero as the velocity increases. Another feature of note is the asymmetry of each voltage spike.

A second measurement of  $U_{PP}$  was planned under a 3000 N load which had to be cancelled due to the measurement electronics breaking at 110 km/h during the first run.

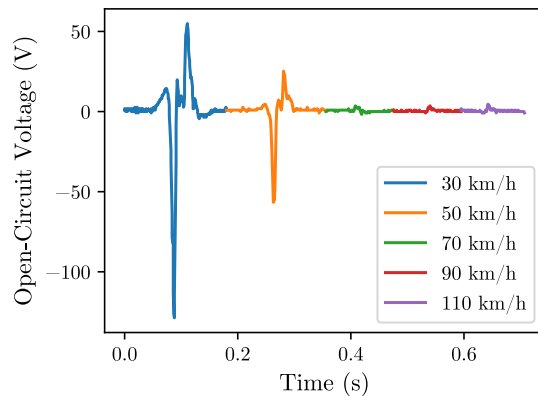


**Figure 4.21:** A spliced measurement series of  $U_{PP}$  measured inside a tire under 1500N load at various speeds.

## 4. Results

---

Since the currents were measured over a longer time span, each measurement was taken at a constant velocity, with the system being reset to zero before starting the next measurement at a new velocity. Due to low measurement resolution, rolling time averages with large windows were employed to eliminate noise. Note the undulating rise in voltage in figure 4.22, this is believed to be a measurement artifact derived from the discrete steps in voltage. To reduce their influence the resulting current was calculated over several undulations to allow the steeper portion to work against the shallower.

During the 10 km/h run a current of 23.47 nA was observed while the 20 km/h run resulted in 11.92 nA. Thus a negative dependence on velocity was seen here in the same manner as for  $U_{PP}$ .

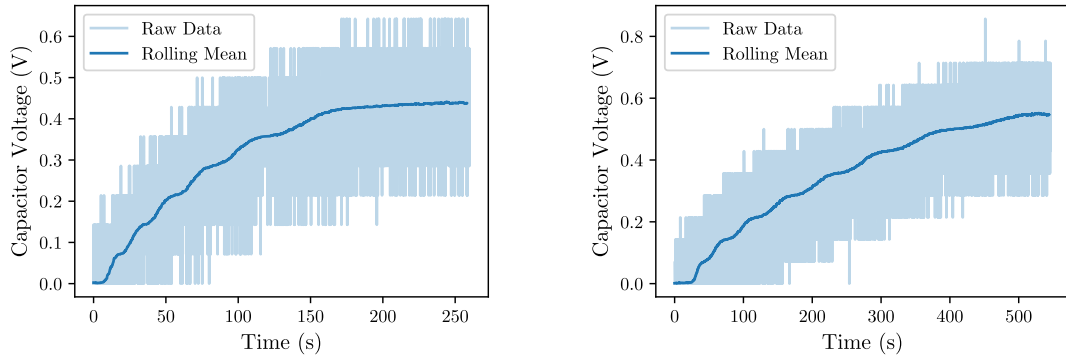


**Figure 4.22:** Capacitor charges over time during a run of 10 km/h (left) and 20 km/h (right). Note the timespan being twice as long during the 20 km/h run.

### 4.2.2.2 Grated sliding mode TENG

The resulting construction is shown in figure 4.23. Two interlaced copper combs act as the two electrodes, encased in two sheets of 25  $\mu\text{m}$  thick Kapton. The slider is built from copper tape fixed onto a sheet of PP.

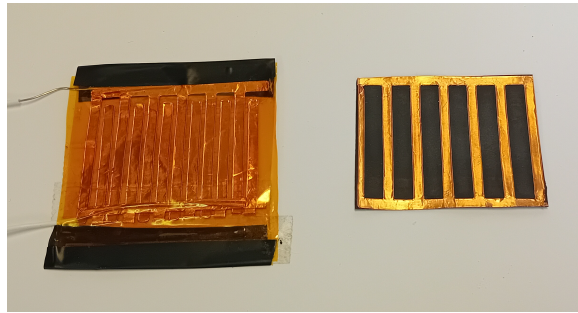


**Figure 4.23:** The grated sliding mode TENG. On the left is the stationary part while the slider is on the right.

Since the measurements of the grated sliding mode TENG were carried out before the modified contact mode, voltage measurements were completed under 1500 and

3000 N loads. However these measurements stopped at 30 km/h to avoid breaking the measurement electronics.

As can be seen in figure 4.24, the grated TENG produced lower voltages than the contact variant. Nonetheless a positive correlation with velocity can be observed where further measurements are needed to investigate this relationship for higher velocities.

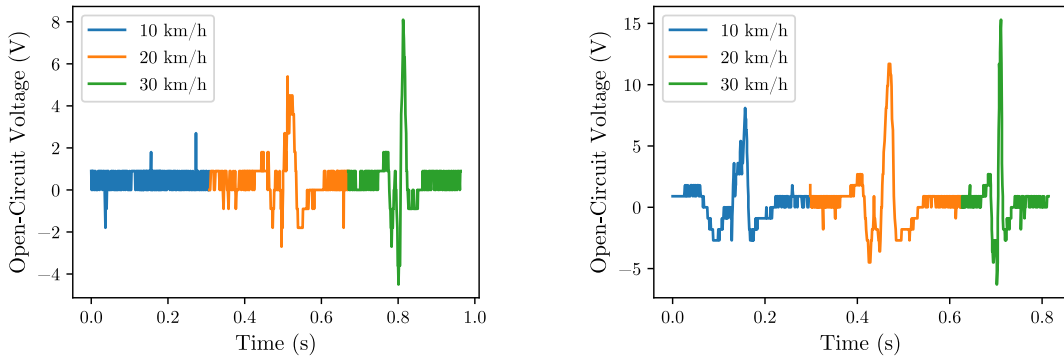


**Figure 4.24:**  $U_{PP}$  measured inside a tire under 1500 N (left) and 3000 N (right) at various speeds.

As was the case with the measured voltages, currents are also lower for the grated sliding TENG than for the modified contact mode TENG. During these measurements it can be difficult to observe any rise in voltage at all without the usage of rolling time averages which can be seen in figure 4.25.

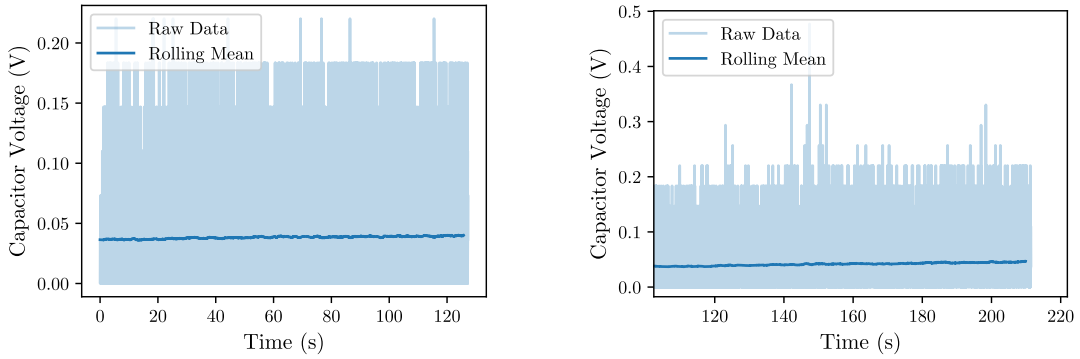


**Figure 4.25:** Capacitor charges over time during a run of 10 km/h (left) and 20 km/h (right).

Currents of 0.176 nA and 0.458 nA were observed during the 10 km/h and 20 km/h respectively. Once again this is lower than the quantities observed for the contact mode although there is a positive correlation with velocity.

#### 4. Results

---

# 5

## Discussion

### 5.1 Simulations

While attempts to understand the effects of design parameters such as geometry on performance characteristics have been made, more work is needed to form a comprehensive framework of TENG design.

#### 5.1.1 Mechanical simulations

There is still a discrepancy between radial displacement  $w$  and harvester actuation  $z$  for the purposes of simulating contact mode harvesters. Comparing the simulated figures 4.3 and 4.4 to measured data in 4.21 shows the predicted flattening of radially operating harvesters as the velocity increases.

Despite the qualitative prediction, both models fail to predict the rate at which the harvester actuation approaches 0. Some tuning of the spring-mass model might produce a more realistic decrease in amplitude by tweaking the spring constant  $k$  and equilibrium height  $r_0$ . Usually this comes with other phenomena such as the small vibrations visible in figure 2.5. Thus the model would have exchanged one unobserved behaviour for another.

As  $U_{OC}$  does not seem to depend too much on the shape of  $z$ , the simulation might as well use the linear short pulse model shown in figure 2.6. Doing so would maximise runtime performance while minimising the amount of implicit assumptions about the physical nature of contact mode harvesters.

In addition to the unknown  $w$ - $z$  coupling, there is some uncertainty from the tire parameters of table 2.2. However  $w(\varphi)$  and  $v(\varphi)$  have been checked against data shown on the test rig at Nokian Tyres to confirm them being within  $\pm 10\%$  of values observed during experiments of section 4.2.2.

#### 5.1.2 Electrical simulations

Among the qualitative predictions posed by the simulations, the most successful one would have to be asymmetric voltage spikes during large transfers of electrons. Even

for linear, symmetric pulses of harvester actuation the produced voltage consists of an asymmetric signal as long as the pulse is sufficiently fast.

More work is needed to confidently be able to verify the saturation shown in figure 4.8 even if the asymmetric curves believed to be the root cause have been observed.

This points to a design problem where the relaxation time of a TENG can be tuned to the system it is attached to in order to maximise the symmetry of each pulse, thus resulting in a greater power output. Primarily this would be adjusted by modifying the dimensions of the TENG but this of course results in a trade off against any possible negative effects due to the change in area.

## 5.2 Physical experiments

A pervasive issue which affected every single measurement is the large dependence on the surface contact between the electrode and dielectric involved in contact electrification.

This is in part a combinatoric problem of material selection. Predicting the performance of combinations from a selection of dielectrics and metals has proven to be troublesome. Figure 4.19 shows conflicting data although some trends can be deduced. Thinner materials seemed to produce higher currents and  $U_{PP}$  as both Kapton and FEP performed better at  $25\mu$  thickness as opposed to their thicker counterparts.

Concluding that thinner dielectrics perform better seems incorrect when considering equation (2.1), which clearly shows that  $U_{OC}$  depends linearly on the dielectric's effective thickness  $\delta$ . Favouring thinner dielectrics is not only theoretically questionable but also contradicted by empirical observations. Throughout the measurements of voltage and current in the robotic actuator, the best performing harvester was consistently recorded. All the top performers were constructed from aluminium and  $127\mu\text{m}$  thick FEP, which, according to the material study, should perform worse than its thinner alternatives.

The best performing harvester tested in the robotic actuator was a  $90\times50\text{ mm}$  aluminium and  $127\mu\text{m}$  FEP sliding mode harvester, actuated along its  $90\text{ mm}$  edge, similar to the one shown in figure 4.10. It produced  $I_{RMS} = 375\text{ nA}$  and  $U_{OC} = 330\text{ V}$ . Unfortunately this is just the beginning pertaining to measurement inconsistencies. The top performing harvester was left in the robotic actuator for a week before being measured again. At that point in time it produced  $I_{RMS} \approx 80\text{ nA}$  and  $U_{OC} \approx 40\text{ V}$ .

One point of concern which has been neglected during measurements is the presence of moisture in the air surrounding the TENG. Relative humidity has been shown to correlate negatively with output voltage and current for TENGs [32]. This effect can reduce the efficiency of each quantity by  $> 50\%$  and as such might be part of the explanation for variations observed on the same TENG over time.

Another factor which is difficult to control for is the flatness of both surfaces involved in the contact electrification. The measurements regarding reverse taping seems to indicate a performance advantage for flatter harvesters. While a flat surface might contribute positively, other research has shown surface fluctuations on a nano scale to improve output performance. Introducing particles on the nano scale or carving patterns onto the TENG surface are a common approach to enhance charge transfer [33].

### 5.2.1 Experiments at RISE

Although the robotic actuator offers significantly greater consistency compared to manual harvesting, it still requires improvements to achieve full reliability.

The torque generated by the continuous servo is inadequate for actuating the harvester at consistent speeds, particularly when using larger TENGs constructed from aluminum and  $127\mu\text{m}$  FEP, which create the highest friction. Naturally this problem is exacerbated under heavier loads which would be of great interest to measure as it provides the most consistent surface interface between the conductor and dielectric.

Moving on from issues related to the measurement setup one must consider the most frequently tested discrepancy between the measurements of this work and theoretical basis which is the sliding direction.

From figure 4.9 in combination with previous findings and theoretical work in the field [34], one would expect the TENG to produce significantly ( $>1$  order of magnitude) more power in the longitudinal direction than the transverse.

However the results shown in figure 4.18 are ambiguous at best. Many TENGs built during the project were measured sliding in both directions. Generally the performance was better in the longitudinal direction or the performance was similar in both directions. This inconsistency with theoretic work done in this report and elsewhere needs further investigation in order to conclusively affirm or deny theory.

While figure 4.18 fails to establish any dependence on sliding direction it does show a convincing, positive correlation of  $U_{PP}$  and  $I_{RMS}$  with the TENG area  $W \cdot L$ . This is a correlation which has previously been observed [35, 36] and is expected due to the transferred charges depending explicitly on the TENG area as per equations (2.3) and (2.6).

### 5.2.2 Experiments at Nokian Tyres

While a sliding mode TENG can actuate past  $x < 0$ , this is clearly not feasible for a contact mode TENG. Therefore, the mounting must ensure a consistent stop at  $z = 0$ , as it is crucial for the two sides of the TENG to make contact with each other.

## 5. Discussion

---

A major point of contention regarding the measurements of the grated sliding TENG is the actual operation mode occurring inside the tire. While the centrifugal forces are large as is evident by the contact mode measurements of figure 4.21, the normal forces of passing the contact patch are large as well. This implies the possibility of a transient stage as the TENG hits the ground where a gap between the conductor and dielectric might occur, leading to a combined sliding and contact mode.

In general the contact mode produces far higher voltage peaks than its sliding counterpart. Thus it is possible for the results of figure 4.24 to be dominated by a contact-separation mechanism rather than a sliding interaction.

Regardless of the positive trends observed for the grated sliding TENG one must consider the inadequacy of the power produced in absolute terms. To have a chance of powering any kinds of energy efficient electronics such as sensors, the current needs to approach  $\approx 1 \text{ mA}$  rather than the  $< 1 \text{ nA}$  measured.

While the root cause of the unexpectedly low performance is unknown, some hypotheses can be formulated in light of measurements at RISE. Due to the ambivalent results on sliding direction the main argument for the geometric structure, namely to maximise  $W/L$ , might fall apart. Unless the structure is shown to significantly contribute to an increase in charge transfer it just results in a sacrifice of triboelectric area while occupying the same footprint.

To some degree the low current could most likely be attributed to the conventional taping of the copper electrodes. Even though the benefits of reverse taping shown in table 4.1 were shown for rectangular “simple” TENGs, there is no obvious reason why producing a flatter harvester would not help a more complex geometry as well.

In addition to reducing  $\delta$  by making a flatter harvester, reverse taping would also greatly reduce the risk of surface wrinkles or folds for the grated sliding TENG. The dielectric covering the comb-like electrodes is a greater risk of forming wrinkles when compared to a dielectric covering a solid rectangle as there are air gaps underneath it. If the electrodes were to be taped onto the film their structural rigidity would help the dielectric to stay flat.

One final effect which has not been measured is the possible contact electrification between the TENG exterior (consisting of PP) and the plastic bag in which it slides. Since the antistatic bag is most likely made of another plastic than PP (usually polyethylene) it is almost certain that some triboelectric charge transfer is occurring. If this were to result in negative charges being transferred onto the PP it could to some degree cancel out the positive charges accumulating on the copper grating.

# 6

## Conclusion

Sliding and contact mode TENGs prove to be a cheap and simple foundation for energy harvesting in mechanically oscillating environments.

Controlling environmental factors like humidity and ensuring optimal material thickness and surface quality are crucial for consistent TENG performance. Improvements in measurement consistency, such as those offered by robotic actuators, are essential. However, the equipment needs further refinement to handle varying loads and maintain reliability.

Mounting electrodes onto the dielectric film seems to increase the generated current as opposed to mounting against the exterior with the dielectric wrapped over it. Additionally a TENG produces more voltage and current the larger its area. For sliding mode TENGs, no dependence on the direction in which it slides could be demonstrated experimentally.

Aluminium electrodes produce more current than identical designs made from copper. This was the case for all dielectric tried with the exception of Mylar. Additionally the aluminium produces a higher voltage for the thinnest films of Kapton and FEP which are promising options for maximum power output.

Later measurements also showed a thicker  $127\ \mu\text{m}$  FEP film to be a well performing dielectric layer.

None of the prototype TENGs constructed during this project achieved a power output in the mW range, which is necessary to power energy-efficient sensors. However, demonstrations showed currents of  $375\ \text{nA}$  and voltages up to  $75\ \text{V}$ , resulting in approximately  $25\ \mu\text{W}$  of power. This indicates that, with further optimization, sliding mode TENGs could potentially reach the required power output. Contact mode TENGs might also reach these levels, but only at low speeds due to the centrifugal force.

## 6. Conclusion

---

# 7

## Future work

This project has made notable progress in developing more advanced harvesters compared to the initial prototypes, many of which have not been detailed in this presentation. However, on a fundamental scientific level, the research has not achieved significant advancements. The inability to experimentally determine how relatively simple factors such as surface area or geometric affect the harvesters is primarily due to inconsistent measurements.

For future research, the development of a more sophisticated measurement rig is essential. This rig should ensure consistent surface contact and be capable of producing oscillations of varying magnitudes and speeds, surpassing the capabilities of the current rotating servo. Such improvements would facilitate a more comprehensive investigation into fundamental questions.

An additional area requiring further attention is the material study, where initial experiments showed that thicker plastic performed poorly but later produced the best harvester. This inconsistency must be addressed. Enhancements in simulation accuracy or the development of new theories are necessary to account for currently ignored effects, as real-life changes in parameters such as width and length do not align with the predicted changes in output performance. Future research should focus on resolving these discrepancies.

## 7. Future work

---

# Bibliography

- [1] S. Beeby, M. Tudor, and N. White, “Energy harvesting vibration sources for microsystems applications,” *Measurement Science and Technology*, vol. 17, no. 12, R175R195, 2006, Cited by: 2620; All Open Access, Green Open Access. DOI: 10.1088/0957-0233/17/12/R01. [Online]. Available: <https://www.scopus.com/inward/record.uri?eid=2-s2.0-33846077160&doi=10.1088/0957-0233/17/12/R01&partnerID=40&md5=a6402d29275280e6ba815c8a872341ea>.
- [2] P. D. Mitcheson, E. M. Yeatman, G. K. Rao, A. S. Holmes, and T. C. Green, “Energy harvesting from human and machine motion for wireless electronic devices,” *Proceedings of the IEEE*, vol. 96, no. 9, pp. 1457–1486, 2008, Cited by: 1591; All Open Access, Green Open Access. DOI: 10.1109/JPROC.2008.927494. [Online]. Available: <https://www.scopus.com/inward/record.uri?eid=2-s2.0-51649122440&doi=10.1109/JPROC.2008.927494&partnerID=40&md5=b51c09a230ee8a6b709f734ec82a50ca>.
- [3] R. Vullers, R. van Schaijk, I. Doms, C. Van Hoof, and R. Mertens, “Micropower energy harvesting,” *Solid-State Electronics*, vol. 53, no. 7, pp. 684–693, 2009, Papers Selected from the 38th European Solid-State Device Research Conference ESSDERC08, ISSN: 0038-1101. DOI: <https://doi.org/10.1016/j.sse.2008.12.011>. [Online]. Available: <https://www.sciencedirect.com/science/article/pii/S0038110109000720>.
- [4] R. Matsuzaki and A. Todoroki, “Wireless monitoring of automobile tires for intelligent tires,” *Sensors*, vol. 8, no. 12, pp. 8123–8138, 2008, Cited by: 105; All Open Access, Gold Open Access, Green Open Access. DOI: 10.3390/s8128123.
- [5] W. Liu and J. Shi, “A dynamics model of triboelectric nanogenerator transducers,” *Nano Energy*, vol. 89, p. 106479, 2021, ISSN: 2211-2855. DOI: <https://doi.org/10.1016/j.nanoen.2021.106479>. [Online]. Available: <https://www.sciencedirect.com/science/article/pii/S2211285521007333>.
- [6] D. Davies, “Charge generation on dielectric surfaces,” *Journal of Physics D: Applied Physics*, vol. 2, no. 11, pp. 1533–1537, 1969, Cited by: 533. DOI: 10.1088/0022-3727/2/11/307. [Online]. Available: <https://www.scopus.com/inward/record.uri?eid=2-s2.0-0041967172&doi=10.1088/0022-3727/2/11/307&partnerID=40&md5=d8d3ec2f809a74f425514e0bc1e11068>.
- [7] J. A. Wiles, B. A. Grzybowski, A. Winkleman, and G. M. Whitesides, “A tool for studying contact electrification in systems comprising metals and insulating polymers,” *Analytical Chemistry*, vol. 75, no. 18, pp. 4859–4867, 2003,

- Cited by: 90. DOI: 10.1021/ac034275j. [Online]. Available: <https://www.scopus.com/inward/record.uri?eid=2-s2.0-0141705528&doi=10.1021%2fac034275j&partnerID=40&md5=b1cf5d98b1248410b9e3b5af3127b88>.
- [8] Y. S. Zhou *et al.*, "In situ quantitative study of nanoscale triboelectrification and patterning," *Nano Letters*, vol. 13, no. 6, pp. 2771–2776, 2013, PMID: 23627668. DOI: 10.1021/nl401006x. eprint: <https://doi.org/10.1021/nl401006x>. [Online]. Available: <https://doi.org/10.1021/nl401006x>.
- [9] S. Trasatti, "Electronegativity, work function, and heat of adsorption of hydrogen on metals," *J. Chem. Soc., Faraday Trans. 1*, vol. 68, pp. 229–236, 0 1972. DOI: 10.1039/F19726800229. [Online]. Available: <http://dx.doi.org/10.1039/F19726800229>.
- [10] K. C., *Introduction to Solid State Physics*. Wiley, 1953. [Online]. Available: [libgen.li/file.php?md5=3e21e1248eaf0aa093e6d52b6c1d4770](http://libgen.li/file.php?md5=3e21e1248eaf0aa093e6d52b6c1d4770).
- [11] M. W. Williams, "Triboelectric charging of insulating polymerssome new perspectives," *AIP Advances*, vol. 2, no. 1, p. 010701, Feb. 2012, ISSN: 2158-3226. DOI: 10.1063/1.3687233. eprint: [https://pubs.aip.org/aip/adv/article-pdf/doi/10.1063/1.3687233/12875553/010701\\_1\\_online.pdf](https://pubs.aip.org/aip/adv/article-pdf/doi/10.1063/1.3687233/12875553/010701_1_online.pdf). [Online]. Available: <https://doi.org/10.1063/1.3687233>.
- [12] W.-G. Kim, D.-W. Kim, I.-W. Tcho, J.-K. Kim, M.-S. Kim, and Y.-K. Choi, "Triboelectric nanogenerator: Structure, mechanism, and applications," *ACS Nano*, vol. 15, no. 1, pp. 258–287, 2021, PMID: 33427457. DOI: 10.1021/acsnano.0c09803. eprint: <https://doi.org/10.1021/acsnano.0c09803>. [Online]. Available: <https://doi.org/10.1021/acsnano.0c09803>.
- [13] S. Niu *et al.*, "Theory of sliding-mode triboelectric nanogenerators," *Advanced Materials*, vol. 25, no. 43, pp. 6184–6193, 2013. DOI: <https://doi.org/10.1002/adma.201302808>. eprint: <https://onlinelibrary.wiley.com/doi/pdf/10.1002/adma.201302808>. [Online]. Available: <https://onlinelibrary.wiley.com/doi/abs/10.1002/adma.201302808>.
- [14] S. Niu and Z. L. Wang, "Theoretical systems of triboelectric nanogenerators," *Nano Energy*, vol. 14, pp. 161–192, 2015, Special issue on the 2nd International Conference on Nanogenerators and Piezotronics (NGPT 2014), ISSN: 2211-2855. DOI: <https://doi.org/10.1016/j.nanoen.2014.11.034>. [Online]. Available: <https://www.sciencedirect.com/science/article/pii/S2211285514002353>.
- [15] Y. Xiong and A. Tuononen, "The in-plane deformation of a tire carcass: Analysis and measurement," *Case Studies in Mechanical Systems and Signal Processing*, vol. 2, pp. 12–18, 2015, ISSN: 2351-9886. DOI: <https://doi.org/10.1016/j.csmpsp.2015.09.001>. [Online]. Available: <https://www.sciencedirect.com/science/article/pii/S2351988615300051>.
- [16] P. Kindt, P. Sas, and W. Desmet, "Development and validation of a three-dimensional ring-based structural tyre model," *Journal of Sound and Vibration*, vol. 326, no. 3, pp. 852–869, 2009, ISSN: 0022-460X. DOI: <https://doi.org/10.1016/j.jsv.2009.05.019>. [Online]. Available: <https://www.sciencedirect.com/science/article/pii/S0022460X0900457X>.
- [17] Y. Wei, L. Nasdala, and H. Rothert, "Analysis of forced transient response for rotating tires using ref models," *Journal of Sound and Vibration*, vol. 320,

- no. 1, pp. 145–162, 2009, ISSN: 0022-460X. DOI: <https://doi.org/10.1016/j.jsv.2008.07.007>. [Online]. Available: <https://www.sciencedirect.com/science/article/pii/S0022460X08006251>.
- [18] S. Sepehri *et al.*, “Gate-folded triboelectric energy harvester for intelligent tires,” *2024 IEEE WIRELESS POWER TECHNOLOGY CONFERENCE*, 2024.
- [19] J. Shao, M. Willatzen, and Z. L. Wang, “Theoretical modeling of triboelectric nanogenerators (TENGs),” *Journal of Applied Physics*, vol. 128, no. 11, p. 111101, Sep. 2020, ISSN: 0021-8979. DOI: 10.1063/5.0020961. eprint: [https://pubs.aip.org/aip/jap/article-pdf/doi/10.1063/5.0020961/13373123/111101/\\_1/\\_online.pdf](https://pubs.aip.org/aip/jap/article-pdf/doi/10.1063/5.0020961/13373123/111101/_1/_online.pdf). [Online]. Available: <https://doi.org/10.1063/5.0020961>.
- [20] R. Foundation. “Rust programming language.” (2024), [Online]. Available: <https://www.rust-lang.org/> (visited on 03/26/2024).
- [21] R. Schwartz. “R&rsorbt2000 oscilloscope.” (2024), [Online]. Available: [https://www.rohde-schwarz.com/se/products/test-and-measurement/oscilloscopes/rs-rtb2000-oscilloscope\\_63493-266306.html](https://www.rohde-schwarz.com/se/products/test-and-measurement/oscilloscopes/rs-rtb2000-oscilloscope_63493-266306.html) (visited on 05/02/2024).
- [22] R. Components. “Mylar film 304x200x0.25mm.” (2024), [Online]. Available: <https://uk.rs-online.com/web/p/plastic-film/7850809> (visited on 05/30/2024).
- [23] Arduino. “Uno r3.” (2024), [Online]. Available: <https://docs.arduino.cc/hardware/uno-rev3/> (visited on 05/30/2024).
- [24] H. Staaf *et al.*, “Simulated and measured piezoelectric energy harvesting of dynamic load in tires,” *Heliyon*, vol. 10, no. 7, e29043, 2024, ISSN: 2405-8440. DOI: <https://doi.org/10.1016/j.heliyon.2024.e29043>. [Online]. Available: <https://www.sciencedirect.com/science/article/pii/S2405844024050746>.
- [25] G. Zhu *et al.*, “A shape-adaptive thin-film-based approach for 50% high-efficiency energy generation through micro-grating sliding electrification,” *Advanced Materials*, vol. 26, no. 23, pp. 3788–3796, 2014. DOI: <https://doi.org/10.1002/adma.201400021>. [Online]. Available: <https://onlinelibrary.wiley.com/doi/abs/10.1002/adma.201400021>.
- [26] R. Components. “Kapton film 304x200x0.025mm.” (2024), [Online]. Available: <https://uk.rs-online.com/web/p/plastic-film/5363946> (visited on 04/24/2024).
- [27] R. Components. “Kapton film 304x200x0.075mm.” (2024), [Online]. Available: <https://uk.rs-online.com/web/p/plastic-film/5363968> (visited on 04/24/2024).
- [28] R. Components. “Fep film 304x200x0.025mm.” (2024), [Online]. Available: <https://se.rs-online.com/web/p/plastic-film/5363980> (visited on 04/24/2024).
- [29] R. Components. “Kapton film 304x200x0.127mm.” (2024), [Online]. Available: <https://uk.rs-online.com/web/p/plastic-film/5363996> (visited on 04/24/2024).

- [30] R. Components. “Peeck plastic film 304x200x0.025mm.” (2024), [Online]. Available: <https://uk.rs-online.com/web/p/plastic-film/7648719> (visited on 04/24/2024).
- [31] R. Components. “Mylar film 304x200x0.025mm.” (2024), [Online]. Available: <https://uk.rs-online.com/web/p/plastic-film/7850802> (visited on 04/24/2024).
- [32] R. F. S. M. Ahmed, S. B. Mohan, S. M. Ankanathappa, M. B. Ravindranath, and K. Sannathammegowda, “Effect of humidity on the performance of polyvinyl chloride based triboelectric nanogenerator,” *Materials Today: Proceedings*, vol. 66, pp. 2468–2473, 2022, 2022 International Conference on Recent Advances in Engineering Materials, ISSN: 2214-7853. DOI: <https://doi.org/10.1016/j.matpr.2022.06.396>. [Online]. Available: <https://www.sciencedirect.com/science/article/pii/S2214785322044145>.
- [33] S. A. Lone *et al.*, “Recent advancements for improving the performance of triboelectric nanogenerator devices,” *Nano Energy*, vol. 99, p. 107318, 2022, ISSN: 2211-2855. DOI: <https://doi.org/10.1016/j.nanoen.2022.107318>. [Online]. Available: <https://www.sciencedirect.com/science/article/pii/S2211285522003962>.
- [34] L. Q. Machado, H. Zhao, M. Amjadi, H. Ouyang, P. Basset, and D. Yurchenko, “Optimisation-driven design of sliding mode triboelectric energy harvesters,” *Nano Energy*, vol. 115, p. 108735, 2023, ISSN: 2211-2855. DOI: <https://doi.org/10.1016/j.nanoen.2023.108735>. [Online]. Available: <https://www.sciencedirect.com/science/article/pii/S2211285523005724>.
- [35] A. Repoulias, I. Logothetis, D. Matsouka, and S. Vassiliadis, “Contact area of electrification materials relating to triboelectric generators: A comparative study,” *Electronic Materials Letters*, vol. 20, no. 3, pp. 283–292, 2024, ISSN: 2093-6788. DOI: [10.1007/s13391-023-00470-z](https://doi.org/10.1007/s13391-023-00470-z). [Online]. Available: <https://doi.org/10.1007/s13391-023-00470-z>.
- [36] D. W. Kim, J. H. Lee, J. K. Kim, and U. Jeong, “Material aspects of triboelectric energy generation and sensors,” *NPG Asia Materials*, vol. 12, no. 1, p. 6, 2020, ISSN: 1884-4057. DOI: [10.1038/s41427-019-0176-0](https://doi.org/10.1038/s41427-019-0176-0). [Online]. Available: <https://doi.org/10.1038/s41427-019-0176-0>.

**DEPARTMENT OF MECHANICS AND MARITIME SCIENCES**

**CHALMERS UNIVERSITY OF TECHNOLOGY**

Gothenburg, Sweden 2024

[www.chalmers.se](http://www.chalmers.se)



**CHALMERS**  
UNIVERSITY OF TECHNOLOGY